# Evaluating plant canopy microclimate using computational fluid dynamics in a plant factory with artificial light

August, 2024

GU XUAN

Graduate School of Horticulture

CHIBA UNIVERSITY

（千葉大学審査学位論文）

# Evaluating plant canopy microclimate using computational fluid dynamics in a plant factory with artificial light

August, 2024

GU XUAN

Graduate School of Horticulture

CHIBA UNIVERSITY

# CONTENTS

# CHAPTER 1.

## Introduction

## 1.1. Plant canopy microclimate in plant factories with artificial light

Currently, agricultural production faces numerous challenges, including population growth, urbanization, unusual weather patterns, uneven distribution of natural resources, and food security (Kozai and Niu, 2019). A plant factory with artificial light (PFAL) is considered a viable solution in which environmental factors, such as temperature, humidity, and light, can be optimally controlled, and the facilities can be built at any location (Kozai et al., 2004). In addition, it achieves year-round crop production (Kozai, 2013a) and provides high-quality plants (Kozai, 2013b).

These facilities enable year-round crop production by precisely regulating environmental factors such as light, temperature, humidity, and $CO_2$ concentration (Kozai et al., 2004). The manipulation of these physical environmental factors directly influences plant growth and development by affecting energy (temperature) and mass ($H_2O$ and $CO_2$) exchange between the microclimate and plants (de Vries, 1963), ultimately impacting crop yield and quality. While PFALs offer superior microclimate control compared to traditional greenhouses, they also entail higher energy consumption and initial investment costs. Therefore, understanding microclimate distribution within plant canopies is essential for designing and operating energy-efficient PFALs.

Figure 1.1 illustrates the energy transfer model for an operational hydroponic container farm, as cited by Liebman-Pelaez et al. (2021). It depicts various components contributing to energy exchange, including $Q_{Cooling}$ (energy removed through the cooling system), $Q_{Envelope}$ (energy exchanged with the envelope through conduction and radiation), $Q_{Infiltration}$ (energy exchanged through infiltration), $Q_{Equipment}$ (internal heat gain due to equipment), $Q_{Lights}$ (internal heat gain due to electric lighting), $Q_{Ventilation}$ (energy exchanged through scheduled ventilation), $Q_{Dehumidifier}$ (sensible and latent gains to the system from the standalone dehumidifier), and $Q_{Plants}$ (sensible and latent gains of the plants with the indoor air). This model is very simple and not realistic, but it offers a comprehensive overview of the energy dynamics for a PFAL.

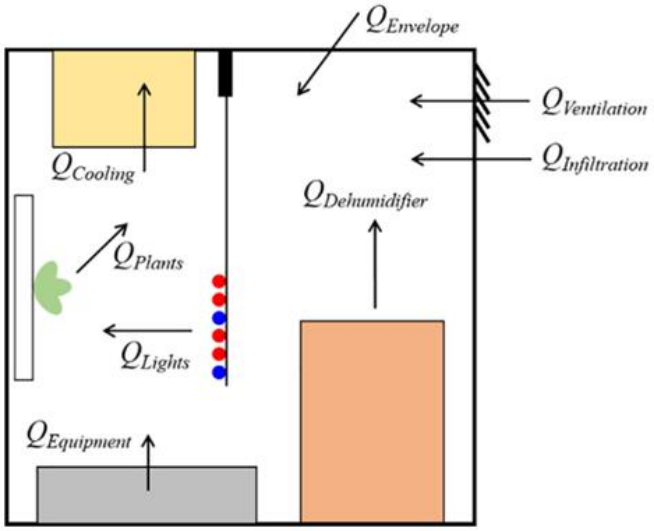


**Figure 1.1** The energy transfer in an operational hydroponic container farm, proposed by Liebman-Pelaez et al. (2021). Arrows point in the direction of positive energy flow.

Figure 1.2 illustrates the energy transfer model within a cultivation shelf of a PFAL. In a single cultivation shelf, essential elements such as water vapor, $CO_2$, $O_2$, and energy for plant growth are primarily supplied through the ventilation system-driven airflow. This model showcases various components involved in energy exchange: The electrical energy from lamps undergoes conversion into photosynthetically active radiation (400–700 nm, PAR), described as light energy ($R_S$), thermal radiation energy ($R_L$), and convection heat ($Q_C$). Additionally, $Q_L$ represents latent heat exchange, while $Q_S$ represents sensible heat exchange between plants and the surrounding air. $Q_W$ accounts for energy exchange through the shelf walls, while $Q_{HVAC}$ exclusively pertains to mechanical air circulation and conditioning for heating and cooling purposes. $Q_E$ denotes the energy produced by other equipments, and $Q_P$ signifies the chemical energy conserved within plants.

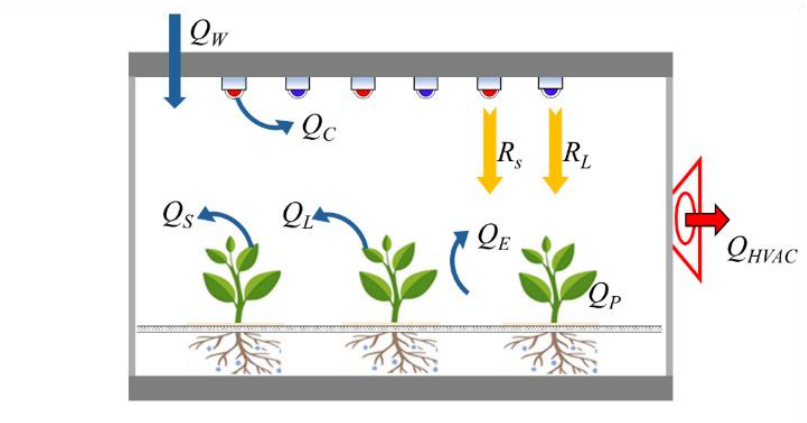


**Figure 1.2** The energy transfer model in a cultivation shelf of a PFAL. Arrows point in the direction of positive energy flow.

However, irregular heat and radiation effects from lamps, coupled with airflow hindrance caused by plant obstructions, contribute to spatial heterogeneity in microclimate within a cultivation shelf. Moreover, the high planting density to increase yield in a PFAL sometimes results in restricted air circulation and non-uniform plant growth. (Yokoi et al., 2008; Goto, 2012). In a PFAL, plant canopy microclimate conditions consisted of light, temperature, humidity, gas, and airflow are critical issues. Changes in these microclimate factors simultaneously impact plant physiological responses, which are maintained within a dynamic equilibrium state (Boulard et al., 2017). The uneven distribution of environmental factors will also result in uneven responses in plant physiological activities, especially transpiration, ultimately affecting plant quality and yield.

To create a suitable environment for plant growth, many studies improved airflow in cultivation shelves by optimizing the inlet and outlet locations of ventilation systems in PFALs (Lim and Kim, 2014; Baek et al., 2016; Niam et al., 2019; Naranjani et al., 2022; Zhang and Kacira, 2022). Recently, more studies used localized airflow control to enhance air velocity (Ahmed et al., 2020; Haibo et al., 2023) and airflow uniformity of a cultivation shelf (Zhang and Kacira, 2022; Okayama et al., 2008; Zhang and Kacira, 2016; Fang et al., 2020; Sohn et al., 2023; Lee et al., 2023; Kang and van Hooff, 2024; Agati et al., 2024). Improving airflow within the plant canopy is currently the effective

method to optimize microclimate in a cultivation shelf. Moreover, increasing airflow within the plant canopy decreases leaf boundary layers, resulting in improving the photosynthesis and transpiration rates of plants and plant growth (Kitaya et al., 2004; Shibuya et al., 2006; Goto and Takakura, 1992; Goto et al., 2014). However, due to the strong coupling relationship among air velocity, temperature, and humidity, focusing solely on controlling air velocity in a cultivation shelf is still insufficient. Additionally, more research is needed to explore methods for optimizing airflow control around plants, taking into account their physiological status.

## 1.2. CFD in simulating plant canopy microclimate

Computational Fluid Dynamics (CFD) is a computerized mathematical simulation tool utilized for solving fluid flow problems and predicting fluid flow and heat transfer phenomena. CFD has matured significantly and is now a powerful design tool widely employed to study various transport phenomena, such as fluid flow, heat, and mass transfer. It provides detailed insights into the spatial and temporal distributions of flow speed, direction, pressure, temperature, and species concentration (Bartzanas et al., 2013).

In greenhouses, modeling the microclimate and transpiration rate distribution based on the mass and energy balance model among the interior environment, exterior environment, and plant interactions has been extensively investigated in the past through CFD tools. Boulard and Wang (2002) pioneered the investigation of crop transpiration heterogeneity by treating crops as porous mediums exchanging latent and sensible heat with their surroundings. Subsequent studies from 2006 to 2017 focused on refining radiative models in CFD simulations to enhance understanding of greenhouse climate dynamics. Fatnassi et al. (2006) applied the Beer law to model radiation transmission through crop canopies, while Bournet et al. (2007) utilized a bi-band radiation model to consider both shortwave (sun) and longwave (sky) radiation transfer. Majdoubi et al. (2009) examined convective and radiative exchanges at the

surface of plastic roof covers. Nebbali et al. (2012) contributed by employing a bi-band discrete ordinates (DO) model to quantify sensible and latent heat transfer between leaves and surrounding air, incorporating both longwave and shortwave radiation fluxes. Building on this groundwork, Boulard et al. (2017) investigated the relationship between microclimate and the transpiration and photosynthesis of plant canopy by modeling 3D radiation and convection transfers within closed-cropped greenhouses. Bouhoun Ali et al. (2018) simulated the microclimate and transpiration of ornamental plants under water restriction conditions.

In PFALs, several studies have utilized similar models to simulate the distribution of air velocity, temperature, and humidity under varying ventilation conditions (Zhang and Kacira, 2022; Kang and van Hooff, 2024). Most studies focused on improving the airflow around plants using the CFD method. Okayama et al. (2008) simulated the airflow near lettuce replicas under different multi-fan systems using cubic lettuce geometry models. Zhang and Kacira (2016) improved the airflow uniformity over a plant canopy through a vertical airflow design, considering the plant canopy surface to be a rough wall. Similarly, Fang et al. (2020) optimized the airflow on the surface of a plant canopy using a horizontal airflow and treating the plant canopy as a porous medium model. In addition, Zhang and Kacira (2022) enhanced the climate uniformity of plant canopies using a CFD model by placing localized air tubes on each shelf. However, compared with mature radiation simulations in greenhouses, the impact of lamp radiation on the microclimate of PFALs is limited.

In previous studies, thermal radiation and PAR emitted by lamps were often oversimplified, merely influencing the surrounding climate through thermal convection (Zhang and Kacira, 2016 and 2022; Fang et al., 2020; Agati et al., 2024) or adding a heat source caused by PAR in the plant canopy (Yu et al., 2023b).

Additionally, in most CFD research, plants were modelled as an implicit porous medium with cuboidal or spherical geometries in greenhouses (Boulard et al., 2017; Bouhoun Ali et al., 2018), orchards (Duga et al., 2015; Hong et al., 2018), and forest areas (Liu et al., 2018; Liu et al., 2021). However, simulating detailed microclimate

patterns in and around plants using this method is challenging because of the lack of plant structural descriptions.

Recently, a few studies have utilized the explicit geometry of trees and shrubs to estimate the effect of plants on flow fields using CFD models (Su et al., 2019; Guo et al., 2021). Detailed flow characteristics can be captured using a CFD model with an explicit geometry of the plants. These previous studies targeted plant growth in external environments, such as forest areas and street canyons. Leaves were simplified in these studies because of their complex plant structures. Leaves are important research objects in agricultural production.

An explicit plant model can be established using direct and reverse modelling of plant components. Direct modelling requires the accurate measurement of each plant component. It is difficult to obtain a detailed description of plant structures (e.g., leaf textures) because of the high spatial complexity of plants (Endalew et al., 2009; Yu et al., 2023a). Reverse modelling can directly extract structures from plants using a 3D scanner and a structure-from-motion (SFM) imaging technique. Several studies have estimated the light environment of plants using SFM (Kim et al., 2020; Ohashi et al., 2020; Saito et al., 2020).

## 1.3. Target type of plant factories with artificial light

This study aimed to analysis the microclimate on a closed-type multilayered cultivation shelf in a PFAL. Compared with the conventional open-type cultivation shelves, the air controlled by an air conditioner system is supplied through the inlet of shelves in the closed-type shelves of the PFAL (Figure 1.3). The air's temperature, humidity, $CO_2$ concentration are controlled by the system. Then the air is flown at the same flow rate by circulation fans. It means that the inlet air condition is almost the same among the multilayered cultivation shelves. The CFD simulation result using a certain shelf can be applied to all the shelves.


**Figure 1.3** The multilayered cultivation system in a plant factory is within an artificial light research unit at Matsudo Campus, Chiba University. A: Conventional open-type cultivation system. B and C: Closed-type cultivation system used in this study. D: Examples of strawberry plants grown on shelves. E: Example of dwarf soybean plants grown on shelves.

## 1.4. Plant transpiration model for CFD simulation

Transpiration plays a crucial role in the water and energy efficiency as it represents the primary mechanism through which plants lose water and exchange energy with their environment. Approximately 99% of the water absorbed by plants is released through transpiration, with only 1% utilized for metabolic processes (Rosenberg et al., 1983). This process is essential for nutrient uptake from the growing media, particularly in hydroponic cultivation where accurate transpiration estimation is vital for effective water management due to the limited water holding capacity and volume of substrates. As mentioned in Section 1.1, transpiration significantly contributes to mass and heat transfer between plants and the microclimate. Therefore, evaluating transpiration is essential for CFD simulation.

Transpiration models of plant canopies can be classified into three main

categories: reference, physical, and data-driven models.

Reference transpiration models are derived from a reference surface, such as grass or alfalfa on the field, assumed to represent a fully irrigated crop canopy. The models are based on climatic formulas calibrated against lysimeter measurements from multiple locations (Allen et al., 1994).

Physical transpiration models are derived from energy balance equations (Stanghellini, 1987). These models do not require crop coefficients but typically involve factors such as stomatal resistance, aerodynamic resistance, and leaf area index, adding complexity to their use.

Data-driven models are employed by statistical regression or machine learning techniques to predict transpiration based on measurement data. This approach often necessitates a large dataset to effectively train the transpiration model (Wang et al., 2021).

In Chapter 3, I selected the physical transpiration model for describing transpiration in plant canopy and incorporated it into the CFD model by particular modifications.

## 1.5. Research objectives and structure of the dissertation

The purpose of this dissertation is to develop a CFD model with realistic plants to evaluate the distribution of plant canopy microclimate and transpiration in PFALs.

Three specific objectives are:

(1) To investigate the effect of inflow velocities and plant canopy structures on the airflow in and around the plant canopy.

(2) To investigate the effect of air parameters on lamp temperature and the microclimate distribution of plant canopies.

This dissertation is composed of four chapters and the contents of each chapter are as follows:

In **Chapter 1**, a general introduction including the background on plant canopy

microclimate, CFD in simulating plant canopy microclimate, and plant transpiration model for CFD simulation. This chapter also identifies knowledge gaps and lists objectives for the research conducted in this thesis. **Chapters 2** and **3** deal with specific objectives (1), and (2), respectively, by developing CFD models integrated with the lamp energy model and the 3D plant microclimate model. In **Chapter 4**, the preceding chapters are summarized, together with presentation of some practical points and perspectives for further research.

# CHAPTER 2.

**Analysis of airflow distribution of plant canopy using a CFD model with realistic plants.**

## 2.1. Introduction

In the PFAL, airflow significantly influences the microclimate in and around a compact plant canopy (Kim et al., 1996; Kitaya et al., 1998) depending on the convection transfer of heat and mass (Korthals et al., 1994). It determines factors such as leaf and air temperatures (Zhang and Lemeur, 1992), humidity, and carbon dioxide concentration. Low airflow cannot mitigate uneven thermal energy from lamps in the vertical direction or homogeneous gas concentrations in the plant canopy. Meanwhile, a high airflow promotes photosynthesis and transpiration rates in plants because it increases gas-exchange rates through a high gas gradient and low boundary layer resistance between plants and the surrounding atmospheres (Kitaya, 2005). However, due to cultivation shelves and plant structures, low airflow often occurs in plant canopy zones, causing an uneven plant growth environment.

Airflow patterns in and around a plant canopy are affected by airflow controls such as inflow velocity and direction. In addition, different layouts, planting densities, and leaf shapes and angles (Yokoi et al., 2008) affect airflow in and around the plant canopy because plant structures are correlated with airflow patterns owing to skin friction and the form drag of plants (Monteith and Unsworth, 2013). However, knowledge regarding the airflow passing through a plant canopy remains limited. To effectively improve the airflow in and around a plant canopy, the ways in which various elements such as inflow velocity and plant canopy structures directly affect airflow patterns and which elements play a dominant role must be understood.

CFD is a powerful tool involving the use of numerical methods to solve fluid flow problems and simulate complex physical phenomena with reasonable accuracy (Zhang et al., 2018). Employing CFD for the analysis of airflow distribution within a plant canopy under diverse conditions emerges as a robust methodology.

The objective of the present study was to develop a CFD model with realistic plant structures to analyze the airflow in and around a plant canopy. In addition, the effects of various inflow velocities and plant canopy structures (e.g., days after sowing (DAS),

arrangement, and leaf veins) on airflow were investigated. Therefore, a CFD model with a 3D realistic plant canopy was developed. Subsequently, experimental measurements were conducted to validate the 3D plant canopy and CFD models. Finally, the airflow in and around the plant canopy was systematically simulated and analyzed under various inflow velocities and plant canopy structures.

## 2.2. Materials and methods

### 2.2.1. Outline of CFD model

I developed an accurate CFD model to simulate the airflow in and around a plant canopy. A commercial CFD program (Fluent, ver. 2021 R2, ANSYS Inc., Canonsburg, PA, USA) was used for the simulations. The simulation results were compared with the experimental results to validate the CFD model. The CFD model was designed to simulate a closed-type cultivation shelf used in the Research Unit for Closed-type Plant Production Systems at Matsudo Campus, Chiba University, Japan (Figures 1.3 and 2.1). The conventional cultivation system in PFALs is an open-type but the modern closed-type cultivation shelf is designed to distribute a same temperature air from an air conditioner unit to each cultivation shelf (Figure 1.3).

The shelf was constructed using blackboards, and four LED lamps (LT-B4600T08-N, OHM ELECTRIC Inc., Saitama, Japan) were installed 0.4 m from the bottom wall. Air flowed through the holes into the cultivation space. Due to the non-uniform distribution of inlet velocity, the velocity was determined by measuring at 12 locations of the inlet area. Approximately 15 d after sowing (DAS), a soybean canopy, cultivated hydroponically in a container was located at the center of the chamber in the y-direction.

### 2.2.2. CFD modelling

#### 2.2.2.1. 3D plant canopy models

##### 2.2.2.1.1. Plant material

I used vegetable soybean (*Glycine max* (L.) Merr., 'Sirojisi'), also called edamame in Japanese as a plant material (Liu et al., 2024). Edamame is harvested and consumed at the immature developmental stage, which occurs when the seeds or pods become larger but do not turn yellow. Their cultivation period from germination is approximately 70 days and is shorter than those of fruit vegetables, such as strawberries and tomatoes. It is common for crops to be cultivated without agrichemicals in a PFAL; therefore, fresh and agrichemical-free edamame could be produced and made available to the market in the future (Liu et al., 2024; Wang, 2018).

##### 2.2.2.1.2. 3D plant canopy model for CFD model validation

The 3D plant canopy model used for the CFD model validation was developed using a reverse modelling method. Plant structures were extracted using the structure-from-motion (SFM) imaging technique, which enabled us to obtain a realistic reconstructed model of plants (Moriondo et al., 2016). This study focused on the leaves as a crucial research object; hence, the vegetative growth stage of soybeans was examined. Figure 2.2 shows the procedure for the 3D modelling of the soybean canopy. First, Metashape (ver.1.8.1, Agisoft LLC, St. Petersburg, Russia) was used to generate dense point clouds with photographs. Secondly, the point dataset was converted into a polygon model. Finally, a 3D plant canopy model was constructed using SpaceClaim (ver. 2021 R2, ANSYS Inc., Canonsburg, PA, USA) from the polyhedron model. The 3D plant canopy model included fine details of the leaves (veins). To reduce the calculation time and skew rate of grids, the stems of the 3D plant model were smoothed.

##### 2.2.2.1.2. 3D plant canopy model for case simulations

A 17 DAS (days after sowing) and a 19 DAS 3D soybean model (Figure 2.3) were established using the method described in Section 2.2.2.1.2. The 3D soybean without

veins was reconstructed from the 3D 17 DAS soybean with veins using SpaceClaim (ver. 2021 R2, ANSYS Inc., Canonsburg, PA, USA). The 3D plant canopy models for the simulations were created by copying a single 3D soybean model (17 and 19 DAS), as shown in Figure 2.3.

#### 2.2.2.2. Simulation domains

##### 2.2.2.2.1. CFD model validation

Simulation domains for CFD model validation were created based on measurements of the shelf with and without plants (Figure 2.1). Computational domains were established using the SpaceClaim software. The simulation domain depicted in Figure 2.1(A) corresponds to condition 1, representing the scenario without soybeans. The simulation domains for conditions 2 and 3, illustrated in Figure 2.1(B), incorporate soybean plants. In these conditions, I did not place any additional objects downstream of the soybean canopy because the impact of downstream airflow on the airflow within and around the plant canopy is relatively small.

##### 2.2.2.2.2. Case simulations

Case simulations were used for studying the effect of inflow velocities and plant canopy structures (e.g., DAS, arrangement, and leaf veins) on airflow in and around plant canopies. In this study, I focused on six scenarios including different inlet air velocities, arrangements of plants, plant sizes, and leaf characteristics. Table 2.1 summarizes the settings of the six cases. Four simulation domains were created for each of the six cases (Figure 2.4). Domain A was used for Cases 1, 2, and 3 to analyze the airflow under different inflow velocities, because the difference among Cases 1, 2, and 3 was the inflow velocities (0.20, 0.50, and 0.80 m $s^{-1}$, respectively). Therefore, the simulation domain of Cases 1, 2, and 3 was the same. The inflow was in the z-direction. Domain B was used for Case 4 to analyze the airflow under different plant arrangements. The staggering distance of the middle row of plants was 0.075 m along the x-direction.

In Domains A and B, the 3D plant canopy consisted of nine identical 17 DAS soybean plants (17 DAS 3D model in Figure 2.3). Domain C was used for Case 5 to examine the airflow alteration with different plant sizes. The 3D plant canopy included nine identical 19 DAS soybean plants (Figure 2.3). Domain D was used for Case 6 to analyze the effect of veins on the airflow. The 3D plant model without veins exhibited a smooth leaf surface (17 DAS 3D model without veins in Figure 2.3). In Table 2.1, LAI ($m^{-2}$ $m^{-2}$) is defined as the ratio of one-sided leaf area to plant ground cover area (0.50 m × 0.52 m).

**2.2.2.3. Transport equations**

The airflow in the computational domain was assumed to be a steady-state, incompressible, viscous, and three-dimensional flow. In this study, the detailed structures of turbulence were not important; therefore, the Reynolds-averaged Navier–Stokes (RANS) equation was applied to model the turbulence. The average mass and momentum equations are as follows:

$$\frac{\partial \rho}{\partial t} + \frac{\partial}{\partial x_i}(\rho u_i) = 0 \quad (1)$$

$$\frac{\partial}{\partial t}(\rho u_i) + \frac{\partial}{\partial x_j}(\rho u_i u_j) = -\frac{\partial p}{\partial x_i} + \frac{\partial}{\partial x_j}\left[\mu\left(\frac{\partial u_i}{\partial x_j} + \frac{\partial u_j}{\partial x_i} - \frac{2}{3}\delta_{ij}\frac{\partial u_i}{\partial x_i}\right)\right] + \frac{\partial}{\partial x_j}\left(-\rho\overline{u_i' u_j'}\right) \quad (2)$$

where $t$ is time (s); $x_j$ is the coordinate in the $j$ direction (m); $u_i$ is the velocity component in the $i$ direction (m $s^{-1}$); $u_j$ is the velocity component in the $j$ direction (m $s^{-1}$); $\rho$ is the density (kg $m^{-3}$); $p$ is the pressure (Pa); $u_j'$ is the fluctuating velocity component in the $j$ direction (m $s^{-1}$); $u_i'$ is the fluctuating velocity component in the $i$ direction (m $s^{-1}$); $\rho\overline{u_i' u_j'}$ is Reynolds stresses; and $\delta_{ij}$ is Kronecker delta.

In several studies, a standard $k$-$\varepsilon$ turbulent model was used to model the airflow through trees due to its robustness, economy, and reasonable accuracy (Endalew et al., 2009; Su et al., 2019). However, the realizable $k$-$\varepsilon$ turbulent model performed the best

among all versions of the *k*-$\varepsilon$ model for separated flows and flows with complex secondary flow features (Fluent User's Guide, 2021). Therefore, it was employed to calculate two additional governing equations for the turbulent kinetic energy ($k$) and turbulent dissipation ($\varepsilon$) of RANS. Because the air temperature difference in the shelf is small (about 9 °C calculated by lamp temperature minus the bottom wall temperature of the shelf), the influence of buoyancy on air movements in the momentum equation was not considered.

Some assumptions relative to leaves' behavior were considered as follows.

(1) In contrast to the larger leaf area, the low thickness of leaves was ignored.

(2) The robust structure of the compact plant canopy presented a formidable barrier to airflow. Consequently, the minute vibrations of the leaves exert minimal influence on airflow and are therefore deemed insignificant.

#### 2.2.2.4. Meshes and boundary conditions

The meshes were generated using Fluent meshing (ver. 2021 R2, ANSYS Inc., Canonsburg, PA, USA). The mesh sizes in all the domains were resolved based on the minimum distance from the surface ($y^+$). In the three models used for validation, the global mesh size was 0.01 m, and the mesh sizes of the containers, stems, and leaves were 0.004, 0.001, and 0.004 m, respectively. The computational grids of the CFD model without and with plants had 0.2 million cells and 1.3 million cells, respectively. The maximum values of skewness were 0.36 and 0.67 for CFD models without and with plants, respectively.

In the four domains, the global mesh size was 0.008 m. The mesh sizes of stems and leaves were 0.0006 and 0.004 m, respectively. The average cell count of Domains A, B, and D was 3.9 million, and the average maximum skewness value was 0.71. The cell count of Domain C was 5.7 million, and the maximum skewness was 0.67. The cells consisted of polyhedrons and hexahedrons. The surface meshes of plants for CFD model validation and case simulation are shown in Figure 2.5.

The independence of the grids was tested to avoid their influence on the simulation

results. The results of the grid independence test for Case 2 are shown in Figure 2.6. Four air velocity profiles with three grid sizes, including 2.1 (coarse), 4.7 (medium), and 6.4 (fine) million, in a plant canopy were compared. The accuracies of the coarse and medium grids were evaluated using the normalized root mean squared error (NRMSE) (Wang and Zhai, 2012):

$$\mathrm{NRMSE} = \frac{3}{r^l - 1}\sqrt{\frac{\sum_{i=1}^{n}[y_1(i) - y_2(i)]^2}{\sum_{i=1}^{n} y_2(i)^2}} \tag{3}$$

where $y_1(i)$ and $y_2(i)$ are the prediction values for the coarse and medium grids, respectively; $r = 2$ is the grid change step which is recommended doubling or halving; $l = 2$ is the order of the numerical scheme which is determined by second-order discretisation schemes in solver setting; and $n = 45$ is the number of predicted values.

In the CFD model, the prediction values of the four lines in Figure 2.6 were collected, and the NRMSEs were compared between the coarse and medium grids, with the fine grid as the base. The NRMSEs of the coarse and medium grids were <10.0%. Both models produced satisfactory simulation results. However, 4.7 million cells (medium grid) were chosen for the superior accuracy in modelling the airflow.

The boundary condition settings were referred to (Zhang et al., 2016; Fang et al., 2020; Fluent User's Guide, 2021; Zhang et al., 2020). The boundary conditions of the CFD models for these cases are summarized as follows: The inlet was set to the air velocity. The turbulence intensity was 5.0%, and the turbulent viscosity ratio was 10. The outlet was set to atmospheric pressure. The pressure at all boundaries of the atmospheric domains was set to zero. The bottom and plant surfaces were assumed to have no-slip walls. The other surfaces were symmetrical planes, in order to avoid the effects of walls on the airflow. The density and viscosity of air were 1.225 kg $m^{-3}$ and $1.789\times10^{-5}$ kg $m^{-1}$ $s^{-1}$, respectively.

#### 2.2.2.5. Solver settings

A pressure-based solver was used to solve the incompressible flows, and the SIMPLE algorithm was used for steady simulations to calculate the pressure-velocity coupling. A least-squares cell-based scheme of Fluent was used for the gradient terms. Second-order discretization schemes were used for pressure, momentum, turbulent kinetic energy, and turbulent dissipation rate. Convergence was assessed by monitoring air velocity on specific locations in the flow field. The convergence criterion of residuals was set to $10^{-3}$ on the mass, momentum, and viscous terms. The solver settings were set with reference to the studies of Zhang et al. (2016), Fang et al. (2020), Zhang et al. (2020), and the Fluent User's Guide (2021). Detailed settings for Fluent calculations are shown in Table 2.2. A computer (HP EliteDesk 800 G5, HP Japan Inc., Tokyo, Japan) with Intel i7-9700 (8 cores, 3.00 GHz, 64 GB RAM) was used to calculate the CFD model. The computing time for solving 5.7 million cells was 1 h using 2 solver processes over 200 iterations.

#### 2.2.2.6. Experimental measurements for CFD model validation

Three different measurements were performed by measuring air velocities on the shelf in Figure 2.1 (condition 1: under 0.6 m $s^{-1}$ inlet velocity without plants; conditions 2 and 3: under 0.6 and 0.8 m $s^{-1}$ inlet velocity with plants, respectively).

A hot-wire anemometer (CLIMOMASTER ® MODEL 6501series, KANOMAX JA-PAN Inc., Osaka, Japan) with a sensor (Range: 0.01–0.99 m $s^{-1}$, Accuracy: ±0.02 m $s^{-1}$ MODEL6543-21, KANOMAX JAPAN Inc., Osaka, Japan) was used to measure the air velocity. Air velocities at 20 different locations were measured in three different measurement conditions. The layout of the measurement points is shown in Figure 2.1. These data were necessary for validating the CFD model and were recorded every second for 15 s. The entire measured dataset was averaged for comparison with the simulation results.

#### 2.2.2.7. Processing Results

The maximum air velocity ($V_{max}$); average air velocity ($V_{avg}$); percentages of cells (PC) with air velocity < 0.20, 0.20 ≤ air velocity ≤ 0.50, and air velocity > 0.50 m $s^{-1}$ and the coefficient of variation (CV) were used to assess overall airflow in and around the plant canopy (shown in Section 2.3.3). The uniformity of the airflow in and around the plant canopy was evaluated using CV, which was used in (Zhang et al., 2016; Zhang and Kacira, 2022). A high value indicated that the air velocity was non-uniform in and around the plant canopy. Stagnant zone distributions and normalized air velocity around leaves were used to visually analyze the airflow in and around the plant canopy. As pointed out by Kitaya et al. (2004), air velocity ≥ 0.20 m $s^{-1}$ inside a plant canopy was better for photosynthesis. A zone where air velocity < 0.20 m $s^{-1}$ was defined as the stagnant zone. A low value indicates that the airflow in the canopy is not good for plant growth. The volumes with air velocity <0.20 m $s^{-1}$ in the plant canopy were calculated by using the ISO-volume method in CFD-Post. The visualized stagnant zone distributions are shown in Section 2.3.4. To clearly observe the airflow intensity around leaves, I calculated the wall shear stress (WSS) of leaves which is the tangential force per unit area exerted by a flowing fluid on the wall. High WSS values are associated with a high local fluid velocity (Wang, 2020). To facilitate a clear comparison of the airflow intensity around leaves for each case, I calculated normalized wall shear stress. The normalized WSS was calculated by $WSS_n = (WSS - WSS_{min})/(WSS_{max} - WSS_{min})$, where WSS (Pa) was the calculated wall shear stress and $WSS_{max}$ (Pa) and $WSS_{min}$ (Pa) were the maximum and minimum WSS, respectively. The normalized air velocities around the leaves are shown in Section 2.3.5.

The $V_{max}$, $V_{avg}$, PC, stagnant zone distribution, and normalized air velocity around the leaves were calculated using CFD-Post (ver. 2021 R2, ANSYS Inc., Canonsburg, PA, USA). The CV was calculated using Python (ver. 3. 10).

## 2.3. Results and discussion

### 2.3.1. 3D plant canopy model validation

The structure of the 3D plant canopy model resembled that of the real plant canopy (Figure 2.2). The location and structure of objects and the location of the camera at a scene were precisely estimated using the SFM imaging technique (Jay et al., 2015). The leaf area of the real plant canopy was 0.09089 $m^2$, as measured using a leaf area meter (LI-3100, LI-COR Inc., Lincoln, Nebraska, USA). The leaf area of the 3D plant canopy was 0.08311 $m^2$, as measured with SpaceClaim, which is slightly lower than 0.09089 $m^2$. The relative error (RE) of the 3D plant canopy was 8.6%. This discrepancy was caused by the rough point dataset of the leaf edges. This result indicates good agreement between the real and 3D plant canopies.

### 2.3.2. CFD model validation

Figure 2.8 compares the simulated air velocities with the measured air velocities at 20 locations in the three models. A remarkable agreement was observed between the simulated and measured air velocities in the CFD model without plants. The mean absolute error (MAE) and mean absolute percentage error (MAPE) of the CFD results were calculated for 20 locations to validate the CFD model (Zhang et al., 2016; Fang et al., 2020). The MAE and MAPE of the CFD model without plants were 0.04 m $s^{-1}$ and 6.7%, respectively. For the CFD model with plants, good agreement between the simulated and measured data was observed. The MAE and MAPE of the CFD model with plants were 0.04 m $s^{-1}$ and 10.1% at the 0.6 m $s^{-1}$ inlet and 0.06 m $s^{-1}$ and 12.7% at the 0.8 m $s^{-1}$ inlet, respectively. Most simulated values were within the maximum and minimum deviations of the measured mean values. The simulated values were slightly higher than the measured values. This discrepancy may be attributed to the underestimation of the leaf area in the 3D plant model. The error of simulation results may be caused by the imprecise setting of the inlet velocity, which was the non-uniform distribution, with a deviation of 4.9%. Furthermore, the experimental shelf was not completely airtight, leading to gas leakage and a lower measured air velocity. In

addition, assuming smooth surfaces for both the shelf and containers may result in high simulated values. The current CFD model can predict air velocity in and around a plant canopy with satisfactory accuracy.

### 2.3.3. Airflow in and around a plant canopy in case simulations

Table 2.3 summarizes the airflows in and around the plant canopy during the simulations with five different numbers of iterations. Each value represents the mean ± standard deviation. In Cases 1–3, with inflow velocities from 0.20 to 0.80 m $s^{-1}$, $V_{max}$ and $V_{avg}$ obviously increased from 0.33 and 0.12 m $s^{-1}$ to 1.21 and 0.55 m $s^{-1}$, respectively. The CV considerably decreased from 103.4% to 86.4%. PC (<0.20 m $s^{-1}$) considerably decreased from 62.3% to 7.2%, and PC (>0.50 m $s^{-1}$) obviously increased from 0.0% to 56.0%. This revealed that a high inflow velocity significantly increased the air velocity and improved uniformity in and around the plant canopy. Case 4, with a staggered layout, slightly increased the $V_{max}$ and $V_{avg}$ from 0.72 and 0.36 to 0.77 and 0.37 m $s^{-1}$, respectively, whereas the CV decreased from 91.1% to 87.1%. PC (<0.20 m $s^{-1}$) diminished with increased PC (0.20–0.50 m $s^{-1}$) and PC (>0.50 m $s^{-1}$). This finding indicates that the air velocity and uniformity in and around the plant canopy were increased by setting a staggered layout of the plants. Case 5, with a big plant geometry, had a high $V_{max}$ of 0.79 m $s^{-1}$ and a low $V_{avg}$ of 0.33 m $s^{-1}$. A rise in PC (<0.20 m $s^{-1}$) was obviously observed from 16.4 to 25.6% with descending PC (0.20–0.50 m $s^{-1}$) and PC (>0.50 m $s^{-1}$). The CV increased from 91.1 to 92.8%. These results indicate that the big plant geometry has negative effects on the air velocity and uniformity in and around the plant canopy. One reason for this could be that the LAI obviously increased as plant geometries became large (Table 2.1), resulting in a small plant-to-space ratio. Case 6 with a smooth leaf surface did not significantly affect $V_{max}$, $V_{avg}$, and PC (<0.20 m $s^{-1}$), PC (0.20–0.50 m $s^{-1}$), or PC (>0.50 m $s^{-1}$). However, the CV decreased substantially from 91.1% to 77.1%, indicating that leaf veins had no significant effect on air velocity, but affected air uniformity. This may be because veins mainly increase skin friction in the plant canopy. Form drag affects the airflow in the

canopy more than skin friction, owing to the angle between the leaf and airflow direction (Monteith and Unsworth, 2013). Leaf veins may affect air uniformity in and around the plant canopy due to the decreased $V_{max}$ and PC (<0.20 m $s^{-1}$).

### 2.3.4. Stagnant zone distributions in case simulations

Figure 2.9 illustrates the distributions of the stagnant zones for the different simulation cases. Cases 1–3 show that the stagnant zones behind the plants were affected by the inflow velocities. The size of the stagnant zones decreased with increasing inflow velocity. However, they were still present in the second and third rows of the plant canopies. Stagnant zones were more evident on the leeward sides of the plants compared with other locations. This is because plants directly block the airflow rather than weaken it, causing a low-airflow zone on the leeward side of the plants (Su et al., 2019). The stagnant zones increased with the depth of the plant canopy. The volume of stagnant zones in the third row was greater than that behind the first row. In Case 4, the staggered arrangement of plants slightly affected the stagnant zones. A slight reduction was detected at the ends of the second and third rows. Case 5 shows that the stagnant zones increased between the two adjacent rows as plant sizes expanded, which is contrary to that at the surface of the top leaves, where the stagnant zones were not distinct. In case 6, the veins of the plants had no significant effect on the stagnant zones. However, slightly smaller stagnant zones were observed on leaves without veins than on leaves with veins (Case 2).

In summary, the number of stagnant zones was mainly influenced by the inflow velocity. The arrangement and growth of plants affected stagnant zones by changing the relationship between plant geometries and cultivation areas.

### 2.3.5. Normalized air velocity around leaves in case simulations

Figure 2.10 shows the normalized air velocities around the leaves in the simulations. In the horizontal inflow cases, the first row had a greater impact on reducing air velocity around the leaves than the second and third rows. The air velocity

distributions around the leaves were similar to those in the stagnant zone. The normalized air velocity increased by 0.25 and 0.75 when the inflow velocity increased to 0.50 and 0.80 m $s^{-1}$ from 0.2 m $s^{-1}$. The inflow velocity of 0.80 m $s^{-1}$ increased the air velocity on the leeward of plants. The air velocity around the leaves on the windward side of the plants was slightly enhanced in Case 4, with a staggered plant canopy in the second row. In Case 5, with a 19 DAS plant canopy, the air velocity around the leaves in the second and third rows increased; however, the stagnant zones also increased (see Table 2.3). This was examined by plotting two plant geometries, as shown in Figure 2.3. The 19 DAS plant had a long internode length (L) at the upper location and a small angle (α) between the leaf and the direction of plant growth. The long L and small α produced high air velocity around leaves. In Case 6, the normalized air velocity on the leaves with smooth surfaces was more uniform than that on the leaves with veins. This result was caused by the increased $V_{max}$ and decreased $V_{avg}$ compared with those in Case 2.

### 2.3.6. Improving airflow in and around a plant canopy

The distribution of stagnation zones significantly affected the air velocity and uniformity in and around the plant canopy. A high inflow velocity was critical for reducing the percentage of stagnation zones. However, excessive inflow velocity can cause excessive air velocity around leaves, which may hinder the photosynthesis and transpiration rates of plants (Korthals et al., 1994). In addition, eliminating stagnant zones with a single inflow direction and different layouts in the plant canopy is difficult. Therefore, it is important to implement a good ventilation method that can effectively eliminate stagnant zones rather than relying solely on increasing the inflow mass. A multidirectional inflow with a suitable air velocity may be effective in improving the air velocity in and around the plant canopy. Okayama et al. (2008) also found that, by studying three inflow patterns, placing fans on both sides to generate inflows in opposite directions provides a more suitable airflow for the plant canopy. Zhang et al. (2016) and Fang et al. (2020) used air ducts with pores to effectively increase the air velocity

at crop canopy surface. Future research will be necessary to explore the influence of air fan and air duct parameters (locations and direction) on airflow in the plant canopy. Although a staggered layout of plants can slightly increase airflow, this may decrease the space utilization of the cultivation area and economic benefits. Therefore, it is not recommended to change the layout of the plant canopy to improve the airflow in and around the plant canopy in a PFAL. As shown in Figures 2.3 and 2.10, the airflow around the leaves varied with plant growth. To ensure optimal ventilation within a plant canopy, it is necessary to adjust the inflow velocity in response to changes in plant canopy structures.

### 2.3.7. Applications of the current CFD model

In contrast to studies that simplified plants to a porous medium (Fang et al., 1994; Zhang et al., 2022; Boulard et al., 2017; Bouhoun et al., 2018), the realistic 3D plant canopy model accurately captures the intricate geometry of leaves, branches, and overall canopy structure. The present CFD model with realistic plants allows quantitative and visual assessment of airflow patterns in and around a plant canopy under different inflow controls and plant structures. Additionally, the current model reduces the need for experimental measurements, as the parameters of the porous medium (e.g. the drag coefficient, porosity, and leaf area density) are unnecessarily measured at different plant canopy structures. The current CFD model quantified the air velocity around the leaves with veins which are not considered in most leaf models (Yu et al., 2023; Roy et al., 2008). Our results indicated that the leaf veins have no significant effect on the whole plant canopy zone; however, they will affect the airflow on the leaf surface. To improve the uniformity of microclimate of the plant canopy in the PFAL, the current CFD model is an effective and powerful method to design airflow controls.

Although the realistic plant model allows for a more quantitative assessment of airflow patterns within a plant canopy compared to the porous medium model, its ability to simulate airflow in complex plant canopies (such as those with leaf interactions and overlaps) remains uncertain. In the future, it is important to comprehend behaviors of

airflow parameters that influence environmental factors such as temperature, humidity, and carbon dioxide concentration surrounding plants because these environmental factors determine plant growth and development.

## 2.4. Conclusions

A numerical simulation using a CFD model with realistic plant structures was developed to study the airflow in and around a plant canopy. Realistic plant structures were established using structure-from-motion imaging. The accuracy of the CFD model was satisfactory when the simulated and measured air velocities were compared. The effects of inflow velocity and plant canopy structure on airflow are summarized as follows: A high inflow velocity significantly increased air velocity and uniformity in the plant canopy. A staggered layout of the plant canopy slightly enhanced the air velocity and uniformity in and around the plant canopy. With big plant structures, the airflow in and around the plant canopy was hindered; however, the air velocity around the upper leaves increased. There is a close relationship between plant structure and airflow around the leaves. The stagnant zones on the leeward side of the plants were difficult to eliminate, even at a high inflow velocity. The CFD model established in this study is an effective and powerful method for exploring the airflow in and around plant canopies in PFALs. Further research is necessary to simulate airflow parameters that influence environmental factors such as temperature, humidity, and carbon dioxide concentration surrounding plants.

## 2.5. Tables and Figures

**Table 2.1** Case settings.

| | Inflow velocity ($m\ s^{-1}$) | Arrangement | DAS[a] (Day) | LAI ($m^{-2}\ m^{-2}$) |
|---|---|---|---|---|
| Case 1 | 0.20 | Square | 17 | 1.00 |
| Case 2 | 0.50 | Square | 17 | 1.00 |
| Case 3 | 0.80 | Square | 17 | 1.00 |
| Case 4 | 0.50 | Stagger | 17 | 1.00 |
| Case 5 | 0.50 | Square | 19 | 1.40 |
| Case 6 | 0.50 | Square | 17 | 0.99 |

[a] represents days after sowing.

**Table 2.2 Detailed settings for Fluent calculations.**

| Item | Setting |
|---|---|
| Models-viscous | Realizable k-e, Enhanced wall treatment, Pressure gradient effects |
| Materials-air | Density (1.225 kg $m^{-3}$), viscosity ($1.789 \times 10^{-5}$ kg $m^{-1}\ s^{-1}$) |
| Materials-shelf | Density (1400 kg $m^{-3}$) |
| Inlet | Velocity magnitude (0.2-0.8 m $s^{-1}$), Turbulent intensity (5%), Turbulent viscosity Ratio (10) |
| Outlet | Gauge pressure (0 Pa) |
| Shelf, lamp, plant | Stationary wall, no slip |
| Pressure-velocity coupling | SIMPLE |
| Spatial discretization | Gradient-least squares cell based, Pressure-second order, Momentum, Turbulent kinetic energy, Turbulent dissipation rate-second order upwind |
| Solution controls | Pressure (0.3), Density (1), Body forces (1), Momentum (0.7), Turbulent kinetic energy (0.8), Turbulent dissipation rate (0.8), turbulent viscosity (1). |

**Table 2.3** Airflow in and around the plant canopy in case simulations.

| | Inflow velocity ($m\ s^{-1}$) | $V_{max}$ ($m\ s^{-1}$) | $V_{avg}$ ($m\ s^{-1}$) | PC (<0.20 $m\ s^{-1}$) (%) | PC (0.20–0.50 $m\ s^{-1}$) (%) | PC (>0.50 $m\ s^{-1}$) (%) | CV (%) |
|---|---|---|---|---|---|---|---|
| Case 1 | 0.2 | 0.33±0.00 | 0.12±0.00 | 62.3±0.02 | 37.7±0.02 | 0.0±0.00 | 103.4±0.00 |
| Case 2 | 0.5 | 0.72±0.00 | 0.36±0.00 | 16.4±0.03 | 58.2±0.01 | 25.4±0.02 | 91.1±0.22 |

| | | | | | | | |
|---|---|---|---|---|---|---|---|
| Case 3 | 0.8 | 1.21±0.00 | 0.55±0.00 | 7.2±0.02 | 36.9±0.03 | 56.0±0.02 | 86.4±0.25 |
| Case 4 | 0.5 | 0.77±0.00 | 0.37±0.00 | 13.1±0.10 | 59.5±0.06 | 27.3±0.04 | 87.1±0.19 |
| Case 5 | 0.5 | 0.79±0.00 | 0.33±0.00 | 25.6±0.15 | 50.4±0.06 | 24.0±0.11 | 92.8±0.12 |
| Case 6 | 0.5 | 0.71±0.00 | 0.36±0.00 | 15.6±0.00 | 58.9±0.00 | 25.4±0.00 | 77.1±0.08 |

Each value represents the mean ± standard deviation (n = 5).

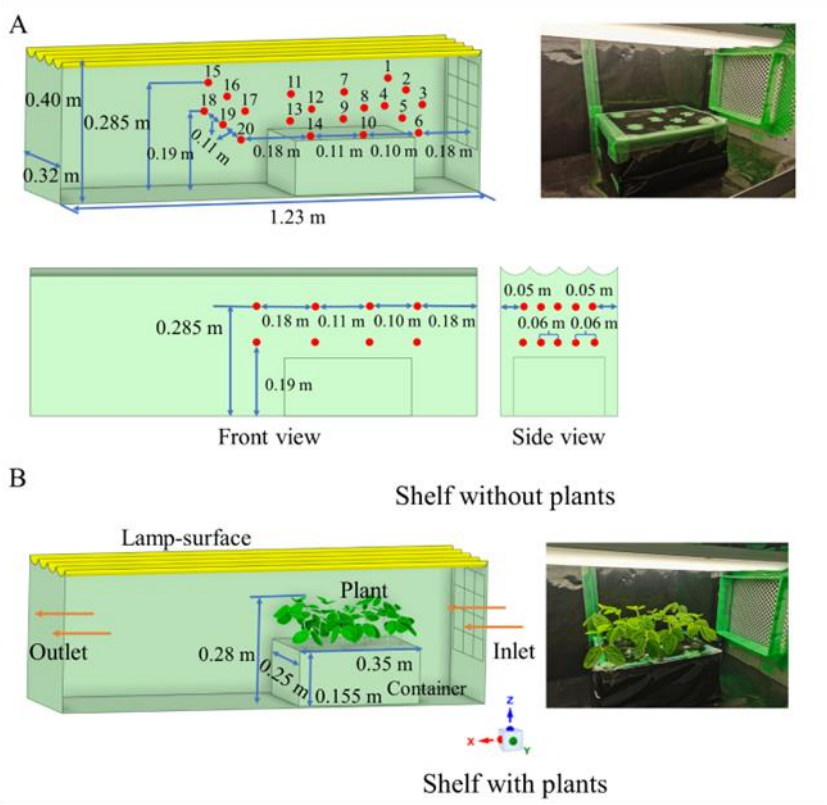


**Figure 2.1** Geometry and photograph of the experimental shelf and sensor location for three measurement conditions for CFD model validation. (A): condition 1; (B): conditions 2 and 3. Numbers 1–20 are locations at which the air velocity in measurement conditions was measured. The cultivation method for soybeans was hydroponics with a container.

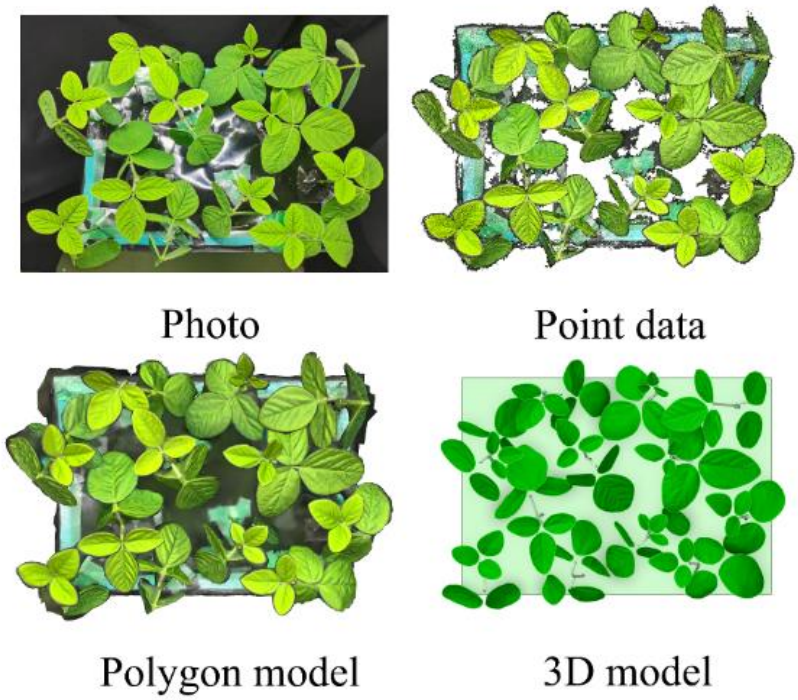


**Figure 2.2** Procedure of 3D modelling of a soybean canopy for CFD model validation. Metashape (ver.1.8.1, Agisoft LLC, St. Petersburg, Russia) generated dense point clouds with photos. The point dataset was converted into a polygon model. SpaceClaim (ver. 2021 R2, ANSYS Inc., Canonsburg, PA, USA) was used to reconstruct the polyhedron model to the 3D plant canopy model.

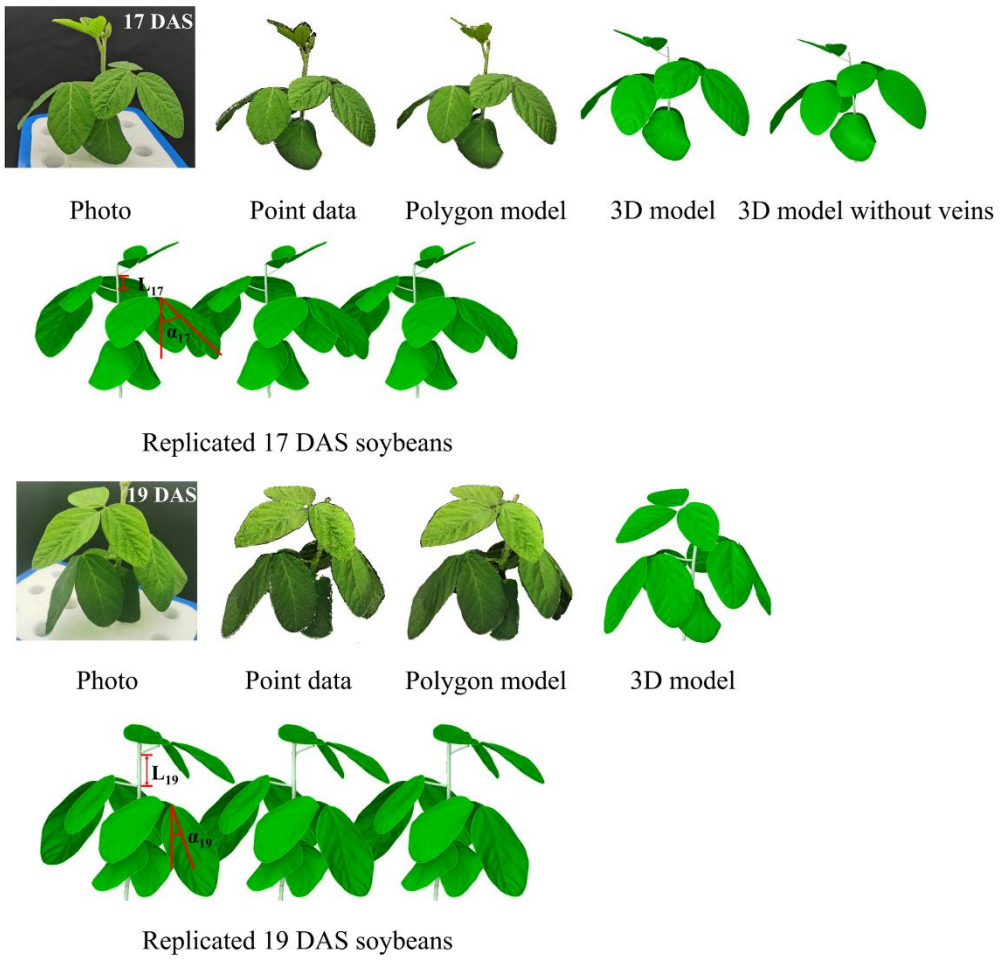


**Figure 2.3** Procedure of 3D modelling of soybean canopies for case simulations. DAS: days after sowing. The 17 DAS and 19 DAS 3D soybean were established by the same method as in Figure 2.2. The 3D soybean without veins was reconstructed from the 3D 17 DAS soybean with veins using SpaceClaim. Soybean canopy models were created by copying a single soybean model.

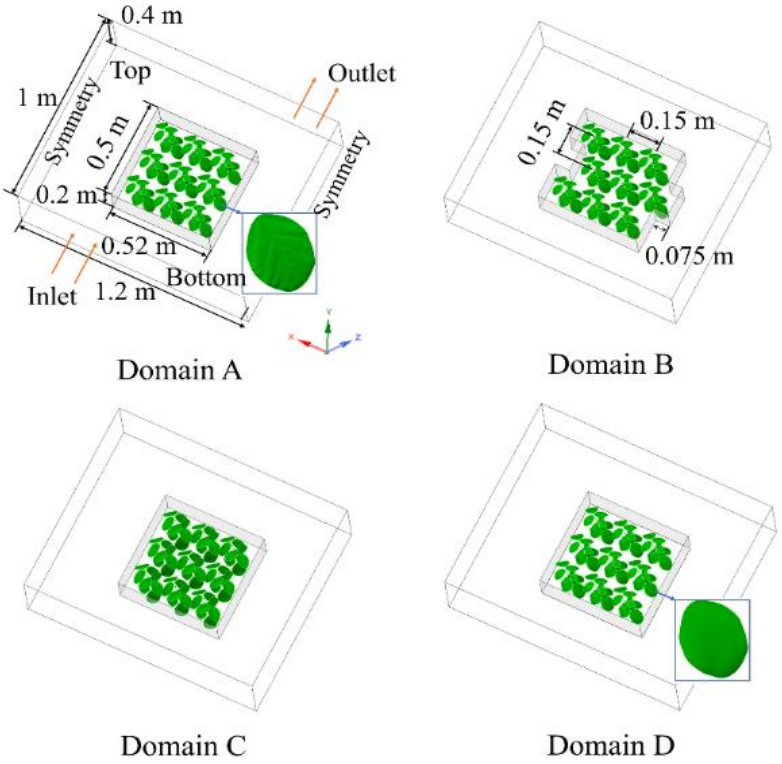


**Figure 2.4** Simulation domains for cases. Domain A for cases 1, 2, and 3, Domain B for case 4, Domain C for case 5, and Domain D for case 6. Cases 1–3 analyzed the effect of inflow velocity on airflow. Case 4 analyzed the effect of plant arrangement on airflow. Case 5 analyzed the effect of plant growth on airflow. Case 6 analyzed the effect of the leaf vein on airflow.

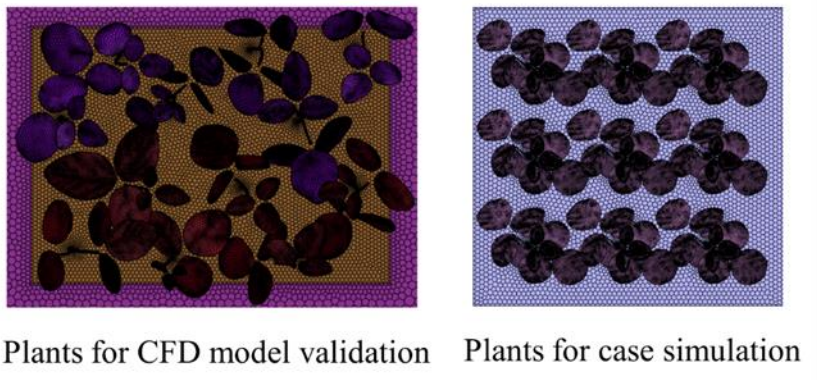


**Figure 2.5** Surface meshes of plants for CFD model validation and case simulation.

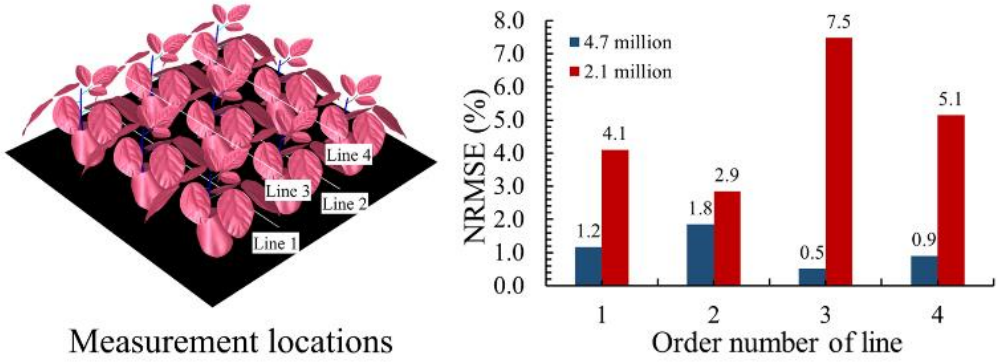


**Figure 2.6** Grid independence test of Case 2. NRMSE: normalized root mean squared error. The 2.1 million and 4.7 million represent the amounts of coarse and medium grids, respectively. Lines 1–4 are the locations of the data collected to calculate NRMSE. The line graph of prediction values of the four Lines are shown in Figure 2.8.

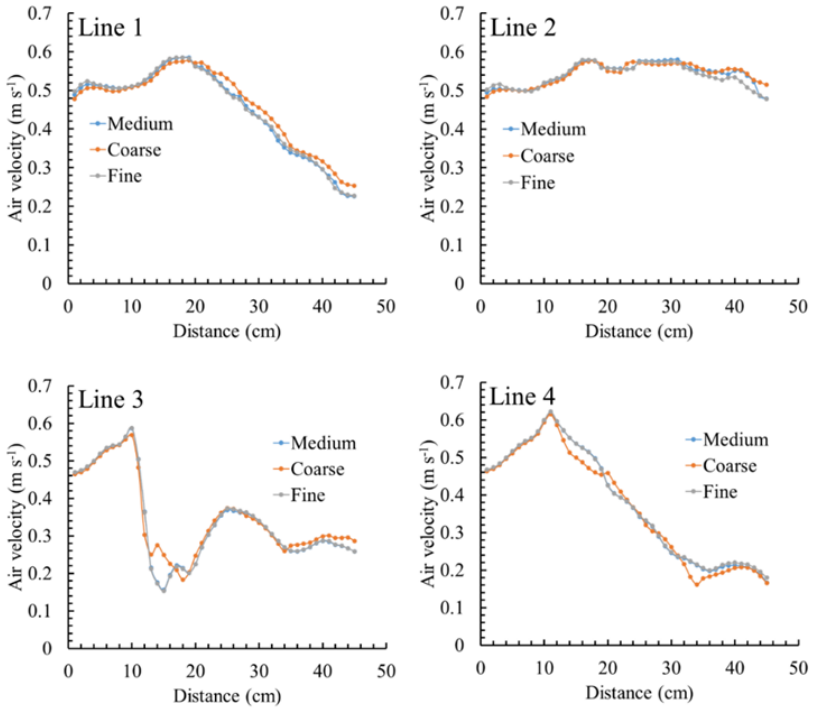


**Figure 2.7** Mesh independence test. Three sizes of meshes (coarse: 2.1 million; medium: 4.7 million; fine: 6.4 million) were compared with the axial air velocity profiles along four lines.

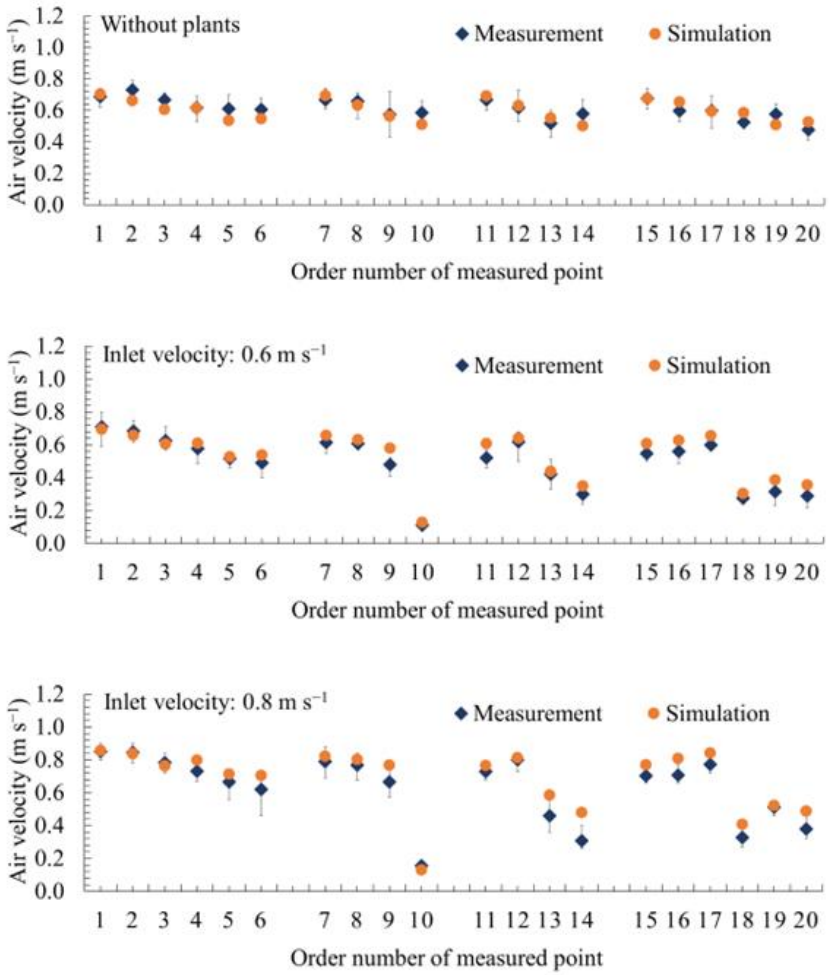


**Figure 2.8** Comparison of the measured air velocity with the simulated data for CFD model validation. The error bars represent the observed minimum and maximum values during the measurement period.

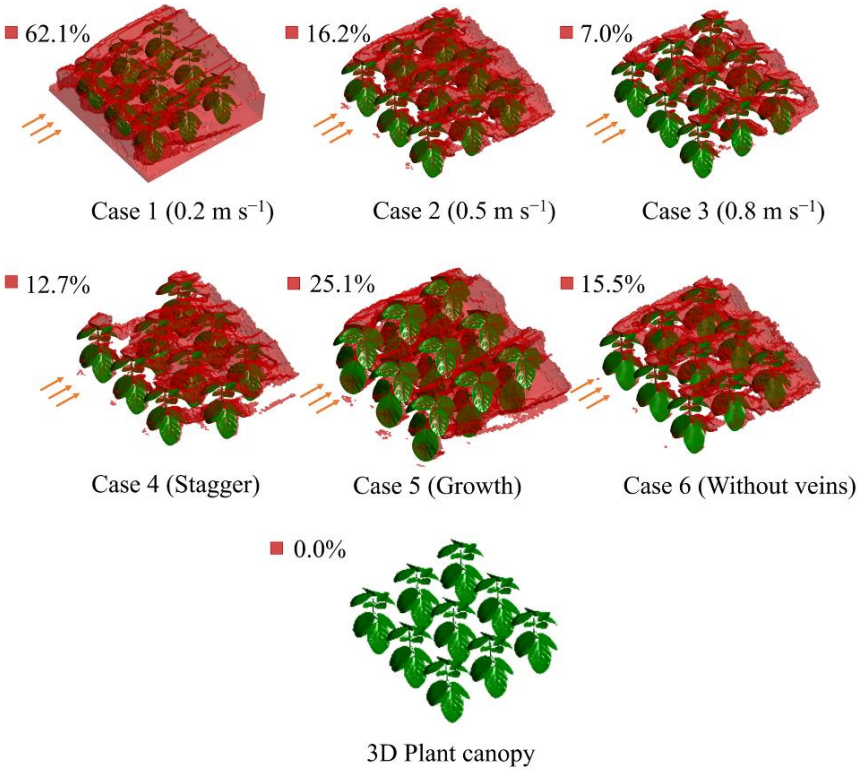


**Figure 2.9** Stagnant zones of 3D distributions in case simulations. The percentages of cells with air velocity <0.20 m $s^{-1}$ [ PC (<0.20 m $s^{-1}$)] are shown. Cases 1–3 analyzed the effect of inflow velocity on airflow. Case 4 analyzed the effect of plant arrangement on airflow. Case 5 analyzed the effect of plant growth on airflow. Case 6 analyzed the effect of leaf veins on airflow. Red zones are with low air velocity (<0.20 m $s^{-1}$). Orange arrows represent inflow direction.

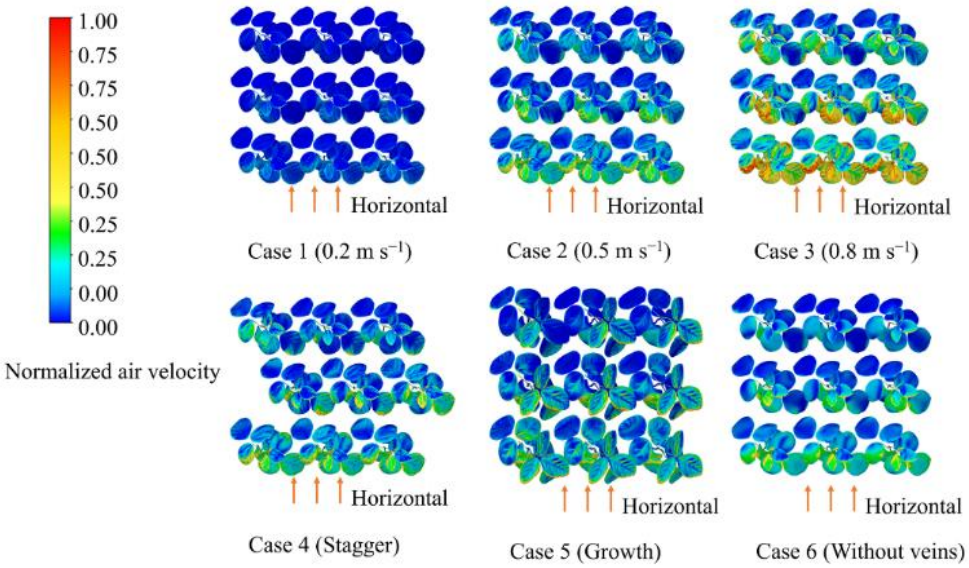


**Figure 2.10** Normalized air velocity around leaves in case simulations. Cases 1–3 analyzed the effect of inflow velocity on airflow. Case 4 analyzed the effect of plant arrangement on airflow. Case 5 analyzed the effect of plant growth on airflow. Case 6 analyzed the effect of leaf veins on airflow. Orange arrows represent inflow direction.

# CHAPTER 3.

**Analysis of lamp temperature and the microclimate distribution of plant canopies under different air parameters using a CFD model with realistic plants.**

## 3.1. Introduction

In the PFAL, physical environmental factors influence plant growth and development by affecting the transfer of energy (temperature) and mass ($H_2O$ and $CO_2$) between the surrounding microclimate and the plants (de Vries, 1963), thereby affecting crop yield and quality. The water vapor, $CO_2$, $O_2$, and energy to plants are predominantly delivered by ventilation system-driven airflow. Most studies have focused on improving the microclimate by controlling the air velocity around plant canopies. However, as described in Chapter 1, low air velocity in plant canopies is difficult to eliminate under different inflow velocities, as well as under a staggered layout of plants. This difficulty arises from the extended recovery process required for the low air velocity on the leeward side of the plants. Moreover, airflow temperature and relative humidity are critical factors. Therefore, to effectively optimize the microclimate in a plant canopy, it is important to quantitatively investigate how airflow parameters, including air velocity, air temperature, and relative humidity, affect the microclimate, and which parameters play a dominant role.

CFD has emerged as a valuable tool for quantitatively analyzing the effects of various factors. Moreover, the CFD method demonstrates robust capability in simulating microclimate distribution within greenhouses (Nebbali et al., 2012; Boulard et al., 2017; Bouhoun Ali et al., 2018) and PFALs (Zhang and Kacira, 2022; Kang and van Hooff, 2024). However, research on how the coupling convective and radiative heat from lamps affects the PFAL microclimate remains limited.

The objective of the present study was to develop a CFD model with a realistic 3D plant canopy based on a crop microclimate model of a cultivation shelf to simulate the distribution of the microclimate and transpiration around a plant canopy. In addition, the developed CFD model with the lamp energy balance predicted the microclimate distribution around a plant canopy under different airflow parameters. Finally, the effects of airflow parameters, namely, velocity, temperature, and relative humidity, on the microclimate in the plant canopies were quantitatively analyzed through regression

analysis.

## 3.2. Materials and methods for validation

### 3.2.1. Experimental measurement

A field experiment was conducted on the cultivation shelf of the multilayered cultivation system of a PFAL research unit at the Matsudo Campus, Chiba University. The shelf was constructed using black film and four LED lamps (LT-B4600T08-N; OHM ELECTRIC Inc., Saitama, Japan). Soybean was selected as the model plant to analyze the microclimate patterns around leaves with multi-layered plant structures. Soybeans exhibit distinct structural features at different growth stages. This study focused on the leaves as a crucial research object; hence, the vegetative growth stage of soybeans was examined. Twenty soybean plants (Sirojisi (*Glycine max* (L.) Merr.) of 18 days after sowing were cultivated in two containers at the center of the shelf. Figure 3.1 shows a photograph and the geometric structure of the shelf. The air velocity, air temperature, and relative humidity of the inlet, surface temperatures of the experimental shelf and lamps (sensor locations at the center of the surfaces), plant transpiration rates, and photosynthetic photon flux density (PPFD) through the lamp surfaces were measured to set the boundary conditions of the CFD model. Air velocities, air temperatures, relative humidity around plants, leaf temperatures, and incident PPFDs of leaf surfaces were measured to verify the CFD model (see Figure 3.1 for details on the sensor locations). Air velocity was measured by a hot-wire anemometer (CLIMOMASTER ® MODEL 6501series, KANOMAX JAPAN Inc., Osaka, Japan) with a sensor (range: 0.01–0.99 m $s^{-1}$, accuracy: ±0.02 m $s^{-1}$, MODEL6543-21, KANOMAX JAPAN Inc., Osaka, Japan). The temperature of air and walls was measured by thermocouples (T-type, range: −200–300 °C). Relative humidity was measured by a thermo-hygro sensor (range: 0–99%, accuracy: ±2.5%, TR-72wf, T&D Corporation, Tokyo, Japan). The cultivation method for soybeans was hydroponics with a container. The amount of water lost from the container was measured using an

electronic balance (shown in Figure 3.4; accuracy: 0.1%; EK-12KI, A&D Co., Ltd., Tokyo, Japan). The transpiration rate of the plants was calculated by dividing the total weight loss of the container by the leaf area during a certain time. The PPFDs on cultivation panel surfaces and leaves were measured with a PPFD sensor (LI-190S, accuracy: ±0.6%, LI-COR Inc., Nebraska, USA) and a photodiode (S1787-08, Hamamatsu Photonics K.K., Shizuoka, Japan), respectively. The incident PPFD on the leaf was estimated by the established relationship between the output voltage of the photodiode and PPFD measured by the PPFD sensor. An infrared thermometer (830-T2, range: −30–400 °C, accuracy: ±1.5 °C, Testo SE & Co. KGaA, Baden-Wurttemberg, Germany) was used to measure leaf temperature.

### 3.2.2. Physical model and numerical modelling

#### 3.2.2.1. Simulation domain

The simulation domains of the cases were established based on the geometry of the cultivation shelf, as described in Section 3.2.1. The simulation domain containing a 3D plant canopy is shown in Figure 3.1. A 3D plant canopy model was developed using the reverse modeling method, which is a structure-from-motion (SFM) imaging technique. Compared to manually drawn methods, the location and structure of objects can be precisely estimated using the SFM imaging technique (Jay et al., 2015). Figure 3.2 shows the modeling procedure for a 3D plant canopy. First, Metashape (ver.1.8.1, Agisoft LLC, St. Petersburg, Russia) was used to generate dense point clouds from photos. Secondly, the point dataset was converted into a polygon model. Finally, a 3D plant canopy model was reconstructed using the polygon model with SpaceClaim (ver. 2021 R2; ANSYS Inc., Canonsburg, PA, USA). The 3D plant model was slightly simplified to reduce the grid skew rate. The leaf area of the real plant canopy was 0.16382 $m^2$ as measured using a leaf area meter (LI-3100, LI-COR Inc., Lincoln, Nebraska, USA). The leaf area of the 3D plant canopy was 0.15997 $m^2$, which was slightly lower than that of the measured data. The relative error (RE) of the 3D plant

canopy was 2.4%. This result indicates good agreement between the real and 3D plant canopies.

#### 3.2.2.2. Transport equation

A CFD program (Fluent, ver. 2021 R2, ANSYS Inc., Canonsburg, PA, USA) was used to predict the microclimate of the plant canopy. A three-dimensional computational model was created based on the measured shelf dimensions (Figure 3.1). The airflow in the computational domain was assumed to be steady-state, incompressible, and viscous. This was assumed to be a mixture of $H_2O$ and air. The mass, momentum, energy, and species mass fraction transport equations were governed (Fluent User's Guide, 2021) by Eqs. **(**1–4):

$$\frac{\partial \rho}{\partial t} + \frac{\partial}{\partial x_j}(\rho u_j) = 0 \quad (1)$$

$$\frac{\partial}{\partial t}(\rho u_i) + \frac{\partial}{\partial x_j}(\rho u_i u_j) = \frac{\partial}{\partial x_j}\left[-p\delta_{ij} + \mu\left(\frac{\partial u_i}{\partial x_j} + \frac{\partial u_j}{\partial x_i}\right)\right] + \rho g_i \quad (2)$$

$$\frac{\partial}{\partial t}(\rho C_p T) + \frac{\partial}{\partial x_j}(\rho u_j c_p T) = \frac{\partial}{\partial x_j}\left(\lambda \frac{\partial T}{\partial x_j}\right) + S_D \quad (3)$$

$$\frac{\partial}{\partial t}(\rho \gamma_n) + \frac{\partial}{\partial x_j}(\rho u_j \gamma_n) = -\frac{\partial j_{n,j}}{\partial x_j} + S_n \quad (4)$$

where $t$ is time (s); $x_j$ is coordinate in the $j$ direction (m); $u_i$ is velocity component in the $i$ direction (m $s^{-1}$); $u_j$ is velocity component in the $j$ direction (m $s^{-1}$); $\rho$ is density (kg $m^{-3}$); $p$ is pressure (Pa); $\delta_{ij}$ is Kronecker delta; $g_i$ is component of the gravity acceleration vector in the $i$ direction (m $s^{-2}$); $C_p$ is the specific heat of air (J $kg^{-1}$ $K^{-1}$); $T$ is temperature (K); $n$ refers to species ($H_2O$ and air); $\gamma$ is species mass fraction (kg $kg^{-1}$); $j_{n,j}$ is the diffusivity of $n$ ($m^2$ $s^{-1}$); $S_D$ is the source term for energy generated by air exchange (W $m^{-3}$); and $S_n$ is the source term for species transport generated by plant transpiration (kg $m^{-3}$ $s^{-1}$). The Reynolds-averaged Navier–Stokes equation with the realizable $k$-$\varepsilon$ turbulent model was applied to model turbulence. This turbulent model calculated two additional governing equations for turbulent kinetic energy ($k$) and

turbulent dissipation ($\varepsilon$), providing superior performance for separated flows and complex secondary flow features (Fluent User's Guide, 2021).

#### 3.2.2.3. Radiative transfer model

Unlike mature studies simulating radiative transfer in greenhouses, radiative transfer in PFALs has generally been ignored. Most studies have focused on convective heat transfer from lamp surfaces to the surroundings (Zhang and Kacira, 2016, 2022; Fang et al., 2020). Thimijan and Heins 1983 reported that for a 46 W fluorescent lamp, 50% of the total energy was emitted as radiation (luminous output and thermal radiation). Therefore, it is necessary to study the radiation transfer of lamps. The energy-transfer mechanisms for the LED lamps in the current CFD model are convection heat transfer, visible-light radiation, and thermal radiation. The wavelength of the visible light radiation was assumed to be in the range of 400–700 nm, corresponding to the wavelength of the PAR. The wavelength of thermal radiation was defined as >700 nm. Radiation transfer within a medium is determined by solving the radiative transfer equation (RTE), which expresses a monochromatic radiative balance along a thin radiation beam. The RTE is expressed by Eq. (5):

$$\frac{dI(\vec{r},\vec{s})}{ds} + (\alpha + \sigma_s)I(\vec{r},\vec{s}) = \alpha {n_r}^2 \frac{\sigma T^4}{\pi} + \frac{\sigma_s}{4\pi}\int_0^{4\pi} I(\vec{r},\vec{s}')\phi(\vec{s}\cdot\vec{s}')d\Omega' \quad (5)$$

where $\vec{r}$ is the position vector; $\vec{s}$ is the direction vector; $\vec{s}'$ is scattering direction vector; $s$ is path length (m); $\alpha$ is absorption coefficient ($m^{-1}$); n is refractive index (considered as 1 in any material); $\sigma_s$ is the scattering coefficient neglected in this study; $\sigma$ is Stefan-Boltzmann constant ($5.67\times10^{-8}$ W $m^{-2}$ $K^{-4}$); $I$ is radiation intensity (W $m^{-2}$), which depends on position ($\vec{r}$) and direction ($\vec{s}$); $T$ is local temperature (K); $\phi$ is phase function; and $\Omega'$ is solid angle. The discrete ordinates (DO) radiation model was used to discretize the RTE using the finite volume method for each direction vector associated with a solid angle (Nebbali et al., 2012). The DO model used a gray band model to calculate the radiation of physically transparent, semitransparent, and

opaque optical media (such as air, glass, and soil surfaces), as previously performed for other climate models in greenhouses (Nebbali et al., 2012; Boulard et al., 2017; Bournet et al., 2007).

The emissivity and absorption of gray body was considered as the same and was independent of wavelength. The radiative properties of shelf surfaces (material: black polyethylene film), lamp surfaces (material: polycarbonate), and leaves were investigated. The emissivity of black polyethylene film, polycarbonate and leaves were 0.94 (Chen and Chen, 2016), 0.98 (Chen et al., 2023), and 0.95 (Hou et al., 2019). The reflectance and transmittance spectra (wavelength: 400–700 nm) of black films and soybean leaves were measured using a UV-visible/NIR spectrophotometer (V-750, JASCO Corporation, Tokyo, Japan) with an integrating sphere unit (ISV-922, JASCO Corporation, Tokyo, Japan). The absorbance and reflectance of the black film were 95.0% and 5%, respectively. The absorptance, reflectance, and transmittance of soybean leaves were 87.0%, 4.5%, and 8.4%, respectively. Because leaf thickness cannot be created in the 3D plant model reconstructed from point cloud data in this simulation, the radiation transmittance for leaves was regarded as zero. The internal emissivity of the shelf and leaf surfaces was set 0.95 in this CFD model. The lamp surfaces were set as semi-transparent surfaces. The internal emissivity of lamps was assumed 1 and direct irradiation (wavelength: 400–700 nm) was specified. The calculation methods for direct irradiation are presented below.

The LED lamp had a 31.9 W power and 5200 lm luminous output with a luminous efficiency of 0.47. The PAR transmitted through the lamp surface was uneven. The radiation intensity in the middle was higher than that on both sides. Therefore, the lamp surface was divided into three parts (1, 2, and 3) to set boundary conditions for the radiation equation (Figure 3.3). The irradiation flux densities ($q_a$ W m$^{-2}$) of parts 1, 2, and 3 were calculated using Eq. (6):

$$q_a = \frac{P_W \eta c_a \frac{b_a}{1 + 1.8 + 3.2}}{\frac{A_l}{3}} \quad (6)$$

where $P_W$ is lamp power (W); $\eta$ is luminance; $a$ is the number of parts; $b_a$ is radiant flux density ratio of parts; $c_a$ is correction coefficient ($c_1$ = 1.43; $c_2$ = 1.10; $c_3$ = 1.03), which was determined by set values/simulation values; and $A_l$ is the lamp surface area (0.1120 $m^2$). The radiant flux ratio of parts 1, 2, and 3 was 1:1.8:3.2 and was determined by measuring PPFD through three parts (Part 1:338.5 μmol $m^{-2}$ $s^{-1}$; Part 2:613.3 μmol $m^{-2}$ $s^{-1}$; Part 3:1074.8 μmol $m^{-2}$ $s^{-1}$). The radiant flux densities of parts 1, 2, and 3 were 96.5, 133.8, and 222.4 W $m^{-2}$, respectively.

#### 3.2.2.4. Crop model

##### 3.2.2.4.1. Energy balance model

Besides the contribution of lamps to the heat load, plants exchange mass and energy with the surrounding microclimate. Radiation transfer through plants is accompanied by the production of water vapor and net sensible heat. The energy balance between the plants and the surrounding environment is explained in Eq. (7):

$$q_i - q_r - q_s - q_l = 0 \quad (7)$$

where $q_i$ is the absorbed PAR flux of leaves (W $m^{-2}$); $q_r$ is the thermal radiation flux of leaves from lamps and surrounding environment (W $m^{-2}$); $q_s$ is the sensible heat flux of leaves by convective heat transfer (W $m^{-2}$); and $q_l$ is the latent heat flux by transpiration of plants (W $m^{-2}$). Since the net energy produced by plant photosynthesis and respiration is small, it was ignored. The sensible heat flux was calculated using Eq. (8):

$$q_s = h_f(T_{leaf} - T_a) \quad (8)$$

where $h_f$ is heat transfer coefficient (W $m^{-2}$ $K^{-1}$); $h_f$ is calculated based on local flow-field conditions including turbulence level, temperature, and air velocity profiles;

$T_{leaf}$ is leaf temperature (K or °C); and $T_a$ is air temperature (K or °C). $q_l$ was calculated using Eq. (9):

$$q_l = h_c ET \tag{9}$$

*ET* is the transpiration rate of plants measured by the method described in 3.2.1. I preliminary measured the plant canopy transpiration rates under various inflow conditions (velocities: 0.2–0.8 m $s^{-1}$; temperatures: 23–25 °C; and humidities: 60–70%) shown in Figure 3.4. The deviation of values of transpiration was smaller than 6.5% under those conditions, therefore, the average value was used in the simulation for each container during the experimental measurement. The ET values were $3.00\times10^{-5}$ kg $m^{-2}$ $s^{-1}$ for right plants and $4.29\times10^{-5}$ kg $m^{-2}$ $s^{-1}$ for left plants. The higher transpiration in the left plants compared to the right plants may be due to lower planting density, higher nutrient solution temperature, and shorter photography duration. Additionally, the left plants grew better than the right plants, as their leaves were larger and more spread out (Figure 3.2). $h_c$ is latent heat of evaporation (2420 kJ $kg^{-1}$). From this relationship, the leaf temperature can be deduced by Eq. (10):

$$T_{leaf} = \frac{q_i - q_r - h_c ET}{h_f} + T_a \tag{10}$$

**3.2.2.4.2. Water vapor transfer model**

The 0-thickness leaf model has two surfaces (adaxial and abaxial surface). The number of stomata in soybean leaves was relatively more on abaxial surface as compared to adaxial surface (Jumrani et al., 2017). Therefore, the water vapor transfer of leaves was described by defining the water vapor source of the cells at the bottom of the leaf abaxial surfaces. The value of the water vapor source in a cell was calculated as the measured transpiration rate (kg $m^{-2}$ $s^{-1}$) × cell area ($m^2$)/cell volume($m^3$). This program was developed and embedded into a CFD model with a user-defined function (UDF). The water vapor source of the whole plant canopy was equaled $5.80\times10^{-6}$ kg

$s^{-1}$ calculated by the measured transpiration rate (kg $m^{-2}$ $s^{-1}$) × the leaf area ($m^2$). The accuracy of the UDF was checked by monitoring the mass (water vapor) source of the CFD model produced by plant transpiration and the value was $5.74\times10^{-6}$ kg $s^{-1}$. The small error may be attributed to the discretization of the leaf surfaces by meshing.

### 3.2.2.5. Air exchange model

Since the cultivation shelf is a semi-closed structure, there is an energy exchange between the internal and external gases. Two data loggers, a computer, and power sources were placed at the exit of the shelf to record the data (with a total power of approximately 150 W). The heat from these items also affects the shelf environment. The energy generated by air exchange ($q_{ae}$) was determined by experimental measurements with the lights turned off. Figure 3.5 shows a photograph of the experimental setup and the measurements. The air temperature and relative humidity at the inlet and outlet were measured ($T_1$–$T_6$). In addition, the wall temperatures of the shelves were measured ($T_7$–$T_{10}$). The energy balance is expressed by Eq. (11):

$$q_{ae} = (h_{out} - h_{in})M - A_w k_w (T_{wall} - T_a) \quad (11)$$

The first term is the total energy absorbed by the internal air, and the second term is the energy absorbed from the walls by the internal air. $h_{out}$ is the specific enthalpy of outlet air (24.4 °C and 57% relative humidity) (J $kg^{-1}$); $h_{in}$ is the specific enthalpy of inlet air (24.0 °C and 58% relative humidity) (J $kg^{-1}$); and $M$ is the mass flow rate (0.081 kg $s^{-1}$). $A_w$ is shelf wall area ($m^2$); $k_w$ is the heat transfer coefficient (W $m^{-2}$ $K^{-1}$) and $T_{wall}$ is wall temperature (°C). Average wall temperature was 24.4 °C. Air temperature was the average of inlet and outlet temperatures (24.2 °C). Considering the small value of $T_{wall}$–$T_a$, the second term was ignored.

### 3.2.2.6. Mesh and boundary conditions

Meshes were generated using Fluent meshing (ver. 2021 R2; ANSYS Inc.,

Canonsburg, PA, USA). The mesh sizes in the simulation domain were determined based on the minimum distance from the surface ($y^+$). The global mesh size was 0.01 m, and the mesh sizes of the containers, stems, and leaves were 0.004, 0.001, and 0.004 m, respectively. The computational grids of the CFD model contained 2.3 million cells with polyhedral and hexahedral elements. The maximum skewness was 0.70. The values of each variable are specified on the boundary surfaces of the simulation domain in Tables 3.1 and 3.2.

#### 3.2.2.7. Solver setting

A pressure-based solver was used to solve the incompressible flows, and the SIMPLE algorithm was used for steady simulations to calculate the pressure-velocity coupling. The least-squares cell-based scheme of Fluent was used as the gradient term. Second-order discretization schemes were used for pressure, momentum, turbulent kinetic energy, turbulent dissipation rate, $H_2O$, energy, and discrete ordinates. Convergence was defined as changes in monitored variables (air velocity, temperature, surface incident radiation) being stable, and the convergence criteria of residuals were set to $10^{-8}$ for the energy term, $10^{-6}$ for the radiation term, and $10^{-3}$ for mass, momentum, and species mass terms.

## 3.3. Materials and methods for cases

### 3.3.1. Physical model and numerical modelling

#### 3.3.1.1. Simulation domain, transport equation, radiative transfer model, and crop model

The simulation domain of the cases was established based on the geometry of the cultivation shelf in the controlled environment room of the Research Unit for Closed-Type Plant Production Systems at Matsudo Campus, Chiba University, as shown in Figure 3.6. The simulation domain was constructed using aluminum and five LED lamp surfaces. A 3D plant canopy without stems was established by randomly assembling

3D plants generated using structure-from-motion (SFM) technology. The stems were ignored because they have a small surface area (2.7%) compared to that of the leaves. The leaf area index (LAI) was 1.5 ($m^2$ $m^{-2}$). The transport equations, radiative transfer model, and crop model of the cases were identical to those used in the validation experiment. The air-exchange model between the shelf and outside was not considered in the simulations because the case simulations was done for the closed-type cultivation system (Figure 1.3 (B, C, E)).

#### 3.3.1.2. Mesh, boundary condition, and solver setting

The global mesh size was 0.01 m, and the mesh size of the leaves and lamp surfaces was 0.004 m. The computational grids of the CFD model contained 1.3 million cells with polyhedral and hexahedral elements. The maximum skewness is 0.73. The independency of meshes on the accuracy of the solution for cases was investigated, with the dependent variable of air velocity, air temperature, and relative humidity. Three sizes of meshes (Mesh 1: 1.3 million; Mesh 2: 2.3 million; Mesh 3: 4.5 million) were compared with the axial air velocity, air temperature, and relative humidity profiles along the shelf length at two poles (Poles 1 and 2 shown in Figure 3.7). The difference between two refinements was evaluated with the normalized root mean squared error (NRMSE) (Wang and Zhai et al., 2012).

$$\mathrm{NRMSE} = \sqrt{\frac{\sum_{i=1}^{n}[y_1(i) - y_2(i)]^2}{\sum_{i=1}^{n} y_2(i)^2}} \tag{12}$$

where $y_1(i)$ and $y_2(i)$ are the prediction values for the coarse and fine grids, respectively; n = 100 is the number of predicted values.

The comparisons of simulations with three meshes at two poles are plotted in Figure 3.7. No obvious differences were observed among the three meshes. The NRMSEs of Mesh 1 and Mesh 2 for air velocity were 1.1% and 0.7%, respectively. The NRMSEs of Mesh 1 and Mesh 2 for air temperature were both 0.0%. The NRMSEs of Mesh 1 and Mesh 2 for relative humidity were both 0.1%. As a result, the mesh resolution of Mesh 1 was chosen to save computational cost.

The values of each variable for the boundary surfaces are specified in Tables 3.2 and 3.3. The shelf surfaces (at the front, back, and bottom) were set as convection, with a 1.6 W $m^{-2}$ K heat transfer coefficient and 23 °C free stream temperature. The material of shelf in cases was aluminum with a low emissivity of 0.03–0.2 (Stanghellini et al., 2019) therefore the internal emissivity was set 0.1. The transpiration rate of plants was assumed to be $3.6\times10^{-5}$ kg $m^{-2}$ $s^{-1}$. I preliminary measured the transpiration rates under Case 14 conditions (Table 3.4). The deviation of the values was smaller than 6.5% and the average value was used in the simulation. Therefore, the heat generation rate of leaves caused by transpiration was −88209 W $m^{-3}$. The coupled algorithm was used for steady-state simulations to calculate pressure-velocity coupling. The other solver settings were identical to those used in the validation experiments.

Most authors imposed the same temperature conditions or convective heat flux on the lamps inside the simulation domain for different cases. These imposed boundary conditions failed to couple radiative and convective exchanges at the lamp surfaces. In this study, the lamp-surface temperatures of the cases were deduced using an energy balance model with an iterative procedure. The energy balance model includes the convective and thermal radiation fluxes exchanged between the lamps and the surrounding environment and the PAR flux of the lamps, as described in Eq. (13).

$$P_W = A_l(h_l(T_{lamp} - T_a) + q_n + \varepsilon_{l,s}\sigma(T_{lamp}^4 - T_s^4)) \quad (13)$$

where $P_w$ is lamp power (31.9 W); $A_l$ is the lamp surface area (m2); $h_l$ is heat transfer coefficient of lamp surfaces (W $m^{-2}$ $K^{-1}$); $T_{lamp}$ is lamp temperature (K); $q_n$ is lamp power for PAR (W); $\varepsilon_{l,s}$ is the emissivity of the lamp to the surrounding environment; and $T_s$ is surrounding wall temperature (K). The residual of the five lamp powers ($5P_w$) was set to 0.5 W. The five lamp powers for the 27 cases are listed in Table 3.4.

### 3.3.2. Case design and statistical analysis

Three airflow parameters were analyzed: air velocity, air temperature, and relative humidity. The different airflow parameters in the plant canopy were controlled by

setting different inflow conditions. Three levels (low, medium, and high) were considered for each inflow parameter. Table 3.4 provides a comprehensive list of inflow parameters along with their corresponding levels; 27 cases were designed and simulated. Regression analysis was conducted to explore the relationship between the response variables (simulation results) and independent variables (inflow parameters). The study focused on nine response variables: leaf temperature ($T_{leaf}$), lamp temperature ($T_{lamp}$), the ratio of convective heat transfer energy to the thermal radiation of lamps ($Q_C/Q_R$), the volumes of zones where air velocity <0.2 m $s^{-1}$ ($V_v$), air temperature >25 °C ($V_T$), and relative humidity >70% ($V_{RH}$), as well as the coefficient of variation (CV) of air velocity ($CV_v$), air temperature ($CV_T$), and relative humidity ($CV_{RH}$) in the plant canopy. $V_v$, $V_T$, and $V_{RH}$ are considered unsatisfactory microclimate zones. The *CVs* were evaluated for the uniformity of the microclimate and defined as the ratio of the standard deviation to the mean value.

## 3.4. Results and discussion

### 3.4.1. PAR validation

The simulated and measured indent PAR of the leaves were compared to evaluate the accuracy of the radiation model shown in Figure 3.8 (a contour of incident PAR and a bar chart comparing the simulated and measured values). The numbers on the contours correspond to the orders of the measured points. The mean absolute errors (MAE) and mean absolute percentage errors (MAPE) of the PAR simulation were 6.3 W $m^{-2}$ and 9.9%, respectively. The results indicate a slight overestimation of the simulated values, which can be attributed to the fact that the measured values were obtained using a light meter with a wavelength range of 400–700 nm. In contrast, the simulated values were calculated based on a broader wavelength range of visible light (360–830 nm). Additionally, the ignored transmitted radiation of the leaves and disparities in the locations of the measured points could impact the simulated and measured values.

### 3.4.2. Leaf temperature validation

Figure 3.9 displays a simulated contour of the leaf temperature along with a bar chart comparing the simulated values with the measured values. The numbers on the leaf temperature contour correspond to the order of the measured points. The MAE and MAPE of leaf temperature were 0.4 °C and 1.4%, respectively. This discrepancy could be attributed to errors in the radiation simulation and the set transpiration fluxes of the leaves. In Section 3.4.1, notably, the simulated PAR was overestimated, likely leading to an overestimation of the simulated leaf temperature. In the crop model, the transpiration flux of leaves within the same cultivation container was assumed to be average. However, the uneven transpiration rate of leaves is influenced by various environmental factors such as radiation intensity, air velocity, air temperature, and relative humidity and plant self-regulation.

### 3.4.3. Validation of air velocity, air temperature, relative humidity and absolute humidity

Figure 3.10 presents a comparison between the measured and simulated air velocities, air temperatures, relative humidities and absolute humidities, with the locations of the measured points illustrated in Figure 3.1. The air velocity, air temperature and relative humidity in the shelf (locations in Figure 3.1) for validation was determined by averaging the data for 15 minutes. Because the inlet conditions were stable, the fluctuations in the environment and plant canopy transpiration on the shelf were small. The boundary values of the CFD model were determined by averaging the measured data. A satisfactory fit was observed between the simulated and measured data at the measured locations. The MAE and MAPE for simulated air velocities were 0.05 m $s^{-1}$ and 11.4%, respectively. Simulated air temperatures exhibited an MAE of 0.2 °C and a MAPE of 0.8%, while simulated relative humidity showed an MAE of 1.0% and a MAPE of 1.8%. The MAE and MAPE for simulated absolute humidity were 0.16 g $m^{-3}$ and 1.2%, respectively. The observed discrepancy in the simulated air

velocities could be attributed to the unsteady-state nature of the inlet air velocity, with a deviation of 4.1% from the mean inlet air velocity. To improve the grid quality, the geometry of the simulation domain and plants were simplified. This led to errors in the simulation results. The differences between the simulated and measured values in air temperature relative humidity and absolute humidity caused by the effect of shielding of the thermocouples and humidity sensors. In the validation measurements, I used a transparent material film and an opaque material film placed above air temperature sensors to confirm the effect of shielding them from radiation. I measured air temperatures with or without these materials at a PPFD of 373 μmol $m^{-2}$ $s^{-1}$ and found 0.3 °C difference between them.

### 3.4.4. Air velocity, air temperature and absolute humidity around the plant canopy

Figure 3.11 shows the distribution of calculated air velocity, air temperature, and absolute humidity at a plane located at the mid-height of the plant canopy. A significant disparity in air velocity was observed between the windward and leeward sides of the plant canopy. This discrepancy raised from the direct obstruction of airflow by the leaves rather than its mere attenuation, resulting in a distinct low-airflow zone on the leeward side of the plants. Furthermore, the areas with a higher leaf density exhibited lower air velocities. A significant difference in air temperature was observed between the inlet and outlet of the shelf. This temperature gradient resulted from the inflow of air absorbing heat from the lamps as it passed through the shelf. The leaves near lamps exhibited higher temperatures due to greater absorption of PAR. Leaf temperature was regulated by transpiration thereby creating some localized low air temperature near leaves. Absolute humidity became higher around the leaves in the leeward because the air gradually absorbed vapor from transpiration along the flow direction.

### 3.4.5. Effects of inflow parameters on lamp temperature, $Q_C/Q_R$, and leaf temperature

Table 3.5 shows the analysis of results for the regression models of lamp

temperature ($T_{lamp}$), leaf temperature ($T_{leaf}$), and $Q_C/Q_R$. $v_{in}$, $T_{in}$, and $RH_{in}$ are linear terms of the regression models. $v_{in}T_{in}$, $v_{in}RH_{in}$, and $T_{in}RH_{in}$ are the 2-way interaction terms. $v_{in}^2$, $T_{in}^2$, and $RH_{in}^2$ are square terms. The residual refers to the difference between the observed and predicted values of the variables. The coded coefficient determines the relative effect of each term on the response variables. The coded coefficients are dimensionless and can be directly compared. The sign of the coded coefficients indicates whether the relationship between a term and the microclimate variables is direct or inverse. The degrees of freedom (DF) represent the number of independent pieces of information available to estimate a particular parameter. The sum of squares (SS) measures the amount of variation for different sources. The F-value was a test for comparing the source's mean square to the residual mean square and P-value was a test for the significance of the source. A significance level of 0.05 ($P < 0.05$) was used to assess the significance of the model terms. The regression models for $T_{lamp}$, $Q_C/Q_R$, and $T_{leaf}$ were significant. This indicates that the regression models can be used to understand the effects of $v_{in}$, $T_{in,}$ and $RH_{in}$ on $T_{lamp}$, $Q_C/Q_R$, and $T_{leaf}$. For the three regression models, the inflow velocity and air temperature were significant, with the inflow velocity being the primary factor. The relative inflow relative humidity is not significant. Increasing the inflow velocity and reducing the inflow temperature lowered the leaf and lamp temperatures and increased $Q_C/Q_R$.

Figure 3.12 displays contour plots of $T_{lamp}$, $Q_C/Q_R$, and $T_{leaf}$ in relation to the significant factors (inflow velocity and temperature). The lamp temperature increased from 35.5 to 44.8 °C with variations in inflow parameters from 0.8 m $s^{-1}$ and 23 °C to 0.2 m $s^{-1}$ and 25 °C. As the inflow velocity increased from 0.2 to 0.5 m $s^{-1}$, the lamp temperature decreased by about 5 °C. Further, as the inflow velocity increased from 0.5 to 0.8 m $s^{-1}$, the lamp temperature decreased by about 2.5 °C. Additionally, a 1 °C increment in inflow temperature (23–24 °C or 24–25 °C) resulted in a nearly 1 °C increase in lamp temperature. $Q_C/Q_R$ increased from 0.39 to 1.30, corresponding to variations in inflow velocity from 0.2 to 0.8 m $s^{-1}$. Below an inflow velocity of 0.57 m $s^{-1}$, the microclimate was primarily influenced by the thermal radiation of lamps,

attributed to a lamp temperature exceeding 37.0 °C. Conversely, when the inflow velocity surpassed 0.57 m $s^{-1}$, convective heat transfer of lamps became the dominant mode of microclimate influence, associated with a lamp temperature below 37.0 °C. Higher lamp temperatures not only elevated air temperatures in proximity to the lamps, but also transmitted heat through thermal radiation to the surrounding space. The $Q_C/Q_R$ increased by approximately 0.49 with the inflow velocity rising from 0.2 to 0.5 m $s^{-1}$ and by about 0.41 with the inflow velocity increasing from 0.5 to 0.8 m $s^{-1}$. Leaf temperature rose from 23.3 to 27.5 °C with a transition in inflow conditions from 0.8 m $s^{-1}$ and 23 °C to 0.2 m $s^{-1}$ and 25 °C. Each 1 °C increase in inflow temperature corresponded to an almost identical 1 °C increase in leaf temperature, a finding consistent with the lamp temperature observations. Specifically, with the inflow velocity increasing from 0.2 to 0.5 m $s^{-1}$, leaf temperature showed a decrease of approximately 1.8 °C. Further, with the inflow velocity rising from 0.5 to 0.8 m $s^{-1}$, the leaf temperature experienced a decrease of about 0.5 °C. The influence of the inflow velocity surpassed that of the inflow temperature on both the lamp temperature and $Q_C/Q_R$. Conversely, the effect of the inflow temperature on the leaf temperature was comparable to that of the inflow velocity. A 1 °C variation in inflow temperature exhibited a lesser impact on leaf and lamp temperatures, as well as $Q_C/Q_R$, in comparison to a 0.3 m $s^{-1}$ alteration in inflow velocity. However, with increasing inflow velocity, the influence of these factors diminishes.

### 3.4.6. Effects of inflow parameters on unsatisfactory microclimate zones ($V_v$, $V_T$, $V_{RH}$)

Table 3.6 presents the analysis of results for the regression models assessing unsatisfactory microclimate zones ($V_v$, $V_T$, and $V_{RH}$). The regression models for $V_v$, $V_T$, and $V_{RH}$ were found to be statistically significant. In the $V_v$ regression model, both inflow velocity and air temperature were significant, with inflow velocity identified as the primary factor. Similarly, for the $V_T$ regression model, both the inflow velocity and temperature were significant, with the inflow temperature being the primary factor. For

the $V_{RH}$ regression model, only the inflow relative humidity was a significant factor. Increasing the inflow velocity and reducing the inflow temperature were associated with a decrease in $V_v$ and $V_T$. Additionally, reducing the inflow relative humidity was associated with a significant decrease in $V_{RH}$. Figure 3.13 illustrates the contour plots of $V_v$ and $V_T$ with significant factors (inflow velocity and temperature) and the contour plots of $V_{RH}$ with inflow velocity, air temperature, and relative humidity. $V_v$ decreased from 0.29 to 0.03 $m^3$ as the inflow parameters transitioned from 0.2 m $s^{-1}$ and 25 °C to 0.8 m $s^{-1}$ and 23 °C. Similarly, $V_T$ decreased from 0.28 to 0.01 $m^3$ under the same inflow parameter changes. Near a low level (0.2 m $s^{-1}$) of the inflow velocity, the interaction of the two parameters was evident with curved contours. It is indicated that the effect of the inflow temperature on $V_T$ was smaller than that at other inflow velocity levels (0.5 and 0.8 m $s^{-1}$ inflow velocity). $V_{RH}$ exhibited a decrease from 0.15 to 0.00 $m^3$ as the inflow relative humidity shifted from 70% to 60%. However, $V_{RH}$ displayed distinct trends at different inflow relative humidity levels. When the inflow relative humidity was below 65%, $V_{RH}$ decreased with increasing inflow velocity. Conversely, when the inflow relative humidity exceeded 65%, $V_{RH}$ increased with a higher inflow velocity. To further elucidate this phenomenon, Figure 3.14 shows the $V_{RH}$ and leaf temperature of the 3D distributions for Cases 6, 15, and 24. These cases had inflow parameters of 0.2, 0.5, and 0.8 m $s^{-1}$, respectively, with consistent inflow relative humidity and temperature (70% and 24 °C). As the inflow velocity increased, the $V_{RH}$ around the leaves became more noticeable. This could be attributed to a decline in leaf temperature resulting from increased inflow velocity, leading to increased humidity around the leaves. Similar phenomena were not observed at 65% and 60% inflow relative humidity. This was probably because, at these inflow relative humidity levels, the effect of leaf temperature on $V_{RH}$ was outweighed by the effect of inflow velocity on $V_{RH}$.

### 3.4.7. Effects of inflow parameters on microclimate uniformity ($CV_v$, $CV_T$, $CV_{RH}$)

Table 3.7 shows the analysis of variance of regression models for microclimate uniformity ($CV_v$, $CV_T$, and $CV_{RH}$). The regression models for $CV_v$, $CV_T$, and $CV_{RH}$ were

significant. Inflow velocity and air temperature significantly affected $CV_v$ and $CV_T$. The inflow velocity, air temperature, and relative humidity significantly affected $CV_{RH}$. The inflow velocity has emerged as the primary factor influencing microclimate uniformity. Increasing the inflow velocity led to enhanced uniformity in air velocity, temperature, and relative humidity within the plant canopy. Lowering the inflow temperature slightly increased the air velocity uniformity, whereas increasing the inflow temperature minimally affected the distribution of air temperature and relative humidity within the plant canopy. Additionally, an increase in relative humidity resulted in higher relative humidity uniformity.

Figure 3.15 illustrates contour plots depicting $CV_v$ and $CV_T$ concerning significant factors (inflow velocity and temperature) and contour plots of $CV_{RH}$ with inflow velocity, temperature, and relative humidity. $CV_v$ decreased marginally from 0.77 to 0.70 as inflow shifted from 0.2 m $s^{-1}$ and 25 °C to 0.8 m $s^{-1}$ and 23 °C. Conversely, $CV_T$ decreased significantly from 0.22 to 0.11 with a transition from 0.2 m $s^{-1}$ and 23 °C to 0.8 m $s^{-1}$ and 25 °C. Similarly, $CV_{RH}$ exhibited a notable decrease from 0.30 to 0.15, as inflow changed from 0.2 m $s^{-1}$, 23 °C, and 60% to 0.8 m $s^{-1}$, 25 °C, and 70%. Although the impact of the inflow parameters on $CV_v$ was not pronounced, it effectively doubled the values of $CV_T$ and $CV_{RH}$.

### 3.4.8. Suggestions for controlling the microclimate of plant canopy

#### 3.4.8.1. Removing heat produced by lamps

Lighting energy is the important heat source which affects the plant canopy microclimate in three ways: photosynthetically active radiation (PAR), thermal radiation, and convection heat transfer. It raises the surrounding air temperature by convection heat transfer. The radiation is absorbed by leaves and converted into heat energy, influencing the leaf temperature and the surrounding air. Figure 3.16 shows the energy transfer between the lights and air in Case 8. The electrical energy (159.1 W) of the five lamps was converted into 84.5 W of thermal energy and 75.1 W of light energy

(PAR). The thermal energy from lamps was transferred to the surrounding air through convection heat transfer (23.7 W of $Q_c$) and to objects in space (plants and other walls), through radiation (60.3 W of $Q_R$). Similarly, the PAR from the lamps radiated to the plants (49.7 W) and other walls (25.4 W). The net radiation absorbed (thermal radiation and PAR) by the other walls was converted into thermal energy and transferred to the air. In contrast, the net radiation absorbed by plants was accompanied by the consumption of latent heat produced by transpiration (76.0 W), and 22.0 W (22%) was transferred to the air. Ultimately, 83.1 W of the total electrical energy (converted into thermal energy) was removed by the airflow. This analysis revealed that the impact of the light source on the microclimate was not limited to the vertical direction (originating from $Q_C$). Light sources also affect other objects in space, primarily plants, through radiation, thereby influencing the microclimate. As mentioned in Section 3.4.4, increasing the inflow velocity and decreasing the temperature improved $Q_C/Q_R$ and decreased the lamp temperature. In simpler terms, a high $Q_C/Q_R$ ratio implies that more energy from the lamps is directly extracted by the air. This results in less thermal radiation from the lamps passing through the canopy, thereby minimizing the impact on the microclimate around the leaves. Plants can adjust their temperature through transpiration to align with the surrounding air. However, it is crucial to note that the heat from the lamps can only be dissipated effectively at high air velocities and low air temperatures. However, excessive inflow velocity and low inflow temperature can hinder plant growth and development. Therefore, it is recommended that different airflow control methods be implemented at the lamp and canopy locations. This suggestion is consistent with the proposal in (Kang and van Hooff, 2024) which found that setting small dimensions of air supply orifice positioned proximally to the LED lamps can effectively remove excess heat and enhance uniformity in air distribution in a small vertical farm.

#### 3.4.8.2. Controlling inflow parameters

The control targets of the environmental parameters in plant regions and inflow

parameters have a strong relationship. In the present study, the target values for air velocity, temperature, and relative humidity in the plant canopy were >0.2 m $s^{-1}$, <25 °C, and <70%, respectively. As mentioned in Section 3.4.5, inflow velocity, inflow temperature, and inflow relative humidity were the most important factors affecting zones with unfavorable air velocity, air temperature, and relative humidity, respectively. Moderate levels of inflow velocity, temperature, and relative humidity (0.5 m $s^{-1}$, 24 °C, and 65%) can substantially reduce unsatisfactory microclimate zones. Therefore, controlling the air temperature and relative humidity of the plant canopy solely by increasing the air velocity is not an appropriate approach. To decrease $V_v$, a high inflow velocity appeared to be the most appropriate. For controlling $V_T$, leaf temperature is a crucial factor. As discussed in Section 3.4.4, the effect of inflow temperature on leaf temperature was comparable to that of inflow velocity. At a high inflow velocity, maintaining a moderate inflow temperature proved to be effective in achieving a leaf temperature close to the target air temperature. Compared with controlling $V_v$ and $V_T$, controlling $V_{RH}$ in the plant canopy is more difficult. This was because the effect of inflow velocity on $V_{RH}$ varied across different levels of inflow relative humidity owing to leaf temperature changes. High levels of inflow relative humidity and air velocity contributed to an increase in $V_{RH}$. Consequently, it is advisable to set the inflow relative humidity below the target level and inflow velocity above the target level. As explained in Section 3.4.6, to control microclimate uniformity ($CV_v$, $CV_T$, and $CV_{RH}$), a high inflow velocity was the most important factor. In conclusion, the optimal inflow parameters were 0.8 m $s^{-1}$ inflow velocity, 24 °C temperature, and 65% relative humidity in the current cases.

### 3.4.9. The simplification of the realistic plant model

Compared to the porous-medium model (Zhang and Kacira, 2022; Boulard et al., 2017), the realistic 3D plant canopy model accurately captures the intricate geometry of leaves, branches, and overall canopy structure. However, its implementation in CFD significantly increases computational time due to its complexity. Therefore, it may be

simplified a realistic plant model. For instance, simplifying leaf veins is suggested. The leaf surfaces in the 3D plant model are smooth, as observed in (Yu et al., 2023a). Our preliminary studies have shown no significant airflow differences between plant canopies with and without leaf veins.

### 3.4.10. Application of the current CFD model based on CFD studies on the urban microclimate

I employed a CFD model with realistic plants to capture detailed microclimate information around the leaves in a PFAL. In Figure 3.11, I observed that the leaves directly blocked the airflow, creating a low-airflow zone on the leeward side of the plants. I also found that the leaves had a cooling effect on the surrounding air due to transpiration. The results show the complex aerodynamic interactions within plant canopies, where leaf morphology and density significantly alter local airflow patterns. There have been many studies on the impact of vegetation on the urban microclimate. According to Pappa et al. (2023), vegetation with large thickness and low permeability in façade greening reduces the air exchange rate of a building model. Gromke et al. (2015) applied transpiration cooling using various vegetations to mitigate outdoor air temperatures in a street canyon. To extend our CFD model to an open-type large cultivation shelf or more variety of plant canopy structures, it is very useful to understand the studies looking into the impact of vegetation on the urban microclimate and studies on the impact of different plant canopy structures.

### 3.4.11. Limitations and further work

#### 3.4.11.1. PAR simulation

Compared with the widely adopted ray-tracing method for light environment simulations (Kim et al., 2020), the DO model solves radiative transfer by discretizing the directions in space. Notably, it also exhibited the capability to simulate radiation transfer in current 3D plant canopies. Moreover, employing this approach significantly

reduces the computation time. However, challenges arise when using the 0-thickness leaf model to simulate radiation transmission through leaves using the DO model. The DO model requires defining the optical properties of the media, including the refractive index and power absorption coefficient, to calculate the radiation transmission of semi-transparent objects with thickness. Many studies have considered plant canopies as semi-transparent porous media and have used the DO model to simulate the radiation transmission through them (Boulard et al., 2017). However, constructing the leaf thickness in the current 3D plant model, which was created from dense point clouds of plants, proved to be challenging. Despite the lower radiation transmittance compared to absorptance in leaves, finding alternative methods is necessary for further improvement.

#### 3.4.11.2. CFD model for simulating the microclimate of the plant canopy

In contrast to the method presented in previous studies (Zhang and Kacira, 2022; Boulard et al., 2017), which simulated the microclimate of the plant canopy using a porous medium model, this study employed a 3D plant canopy model to capture detailed microclimate information around the leaves. Moreover, compared to the approach (Roy et al., 2008; Yu et al., 2023a), that simulated the microclimate around leaves with thickness, this study introduced a leaf surface model without thickness. This improvement enhanced the grid quality and facilitated microclimate analysis in plant canopies with a high LAI. In addition, this CFD model used the DO radiation model and an iterative procedure to predict the lamp and leaf temperatures under different conditions. However, limited dynamic interactions between plant transpiration and the surrounding climate were not considered in the CFD model. Compared to understanding microclimate parameters, the prediction of plant transpiration or photosynthesis offers a direct assessment of plant growth status. Additionally, a deeper understanding of the dynamic interactions between plant transpiration, photosynthesis, and microclimate may facilitate the precise control of the microclimate of the plant canopy. Future studies will enhance the current CFD model to simulate leaf-

microclimate interactions in 3D plants.

The differences in plant structures will also significantly affect the microclimate in the plant canopy. In this study, the model plant was soybean with multi-layered and horizontal leaf structures. Previous studies found that the ventilation rate in the plant canopy with vertical leaves (such as rice) was higher than in the plant canopy with horizontal leaves (such as tomato and soybean) even at high planting densities (Yokoi et al., 2008). Additionally, the airflow in and around the plant canopy was higher in the spinach canopy with more vertical leaf angles than in the qing-geng-cai canopy (Yokoi et al., 2008). Consequently, excessive inflow velocity may not be suitable for canopies with more vertical leaf angles, as it can elevate air velocities around the leaves, potentially hindering plant photosynthesis and transpiration rates (Korthals et al., 1994).

#### 3.4.11.3. Airflow control in the cultivation shelf

Previous studies indicated that inflow position significantly affected the microclimate of the plant canopy (Ahmed et al., 2020; Okayama et al., 2008; Zhang and Kacira, 2016; Fang et al., 2020). In addition, the differences in plant structures will also affect the microclimate in the plant canopy. For example, soybean studied in the present study, leaf lettuce, spinach, and strawberry have different plant structures. Additional research is required to explore methods for optimizing the airflow control on cultivation shelves for different plants. For example, the optimal inflow parameters for the different plant canopies and lamps, including the inflow intensity and angle, need to be clarified. Furthermore, it is crucial to design a new airflow control method that optimizes microclimate conditions and enhances photosynthesis and transpiration in the different plant canopies.

## 3.5. Conclusions

The present study provides a 3D CFD model incorporating a detailed soybean canopy to quantitatively analyze the spatial microclimate under different inflow

parameters on a PFAL shelf. The CFD model was validated against physical field experimental data and accurately described the PAR, leaf temperature, air velocity, temperature, and relative humidity distributions in the plant canopy. The results showed that the inflow velocity and temperature significantly affected the lamp temperature, ratio of convective heat transfer energy to the thermal radiation of lamps, and leaf temperature. Inflow velocity, temperature, and relative humidity exerted more significant effects on air velocity, temperature, and relative humidity than on the other variables in the plant canopy. The inflow velocity significantly improved the uniformity of the air velocity, air temperature, and relative humidity in the plant canopy. Different airflow control methods are recommended at the lamp and canopy locations. The most optimal inflow parameters for this study were identified as 0.8 m $s^{-1}$, 24 °C, and 65% relative humidity. The dynamic interactions between plant transpiration and the surrounding climate were not considered in the current CFD model. The prediction of plant transpiration or photosynthesis offers a direct assessment of plant growth status. Moreover, understanding the interactions between transpiration, photosynthesis, and microclimate can enhance the precise control of the plant canopy environment. Future studies should focus on optimizing airflow control and improving photosynthesis and transpiration in plant canopies by developing a CFD model with realistic plants.

## 3.6. Tables and Figures

**Table 3.1** Boundary conditions of the simulation domain for validation.

| Location | Momentum equation | Energy equation | Radiation equation | Species equation |
|---|---|---|---|---|
| Shelf, container | No-slip | Measured wall temperature (26.1 °C–31.0 °C) | Emissivity (0.95) | Zero diffusive flux |
| Lamp | No-slip | Measured wall temperature (39.0 °C of Parts 1, 2; 39.5 °C of Part 3) | Direct irradiation (Section 3.2.2.3) Emissivity (1.00) | Zero diffusive flux |
| Leaf | No-slip | Coupling, Thickness (0.001 m) Heat generation rate (−72600 W $m^{-3}$ of right plants; −103818 W $m^{-3}$ of left plants) | Emissivity (0.95) | Water vapor source |
| Stem | No-slip | Via system | Emissivity (0.95) | Zero diffusive flux |
| Inlet | Measured inlet velocity (0.6–0.8 m $s^{-1}$) | Measured air temperature (24.5 °C and 25.0 °C) | Emissivity (0.00) | $H_2O$ mole fraction: 0.01821 |
| Outlet | Atmospheric pressure | Measured outside air temperature (27.0 °C) | Emissivity (0.50) | Zero diffusive flux |

**Table 3.2** Material parameters of boundary.

| Material | Density (kg $m^{-3}$) | Specific heat (J $kg^{-1}$ $K^{-1}$) | Thermal conductivity (W $m^{-1}$ $K^{-1}$) | Viscosity (kg $m^{-1}$ $s^{-1}$) | Mass diffusivity ($m^2$ $s^{-1}$) |
|---|---|---|---|---|---|
| Fluid flow | Incompressible ideal gas | Mixing law, Kinetic theory | Mass-weighted mixing law, Kinetic theory | Mass-weighted mixing law, Kinetic theory | Kinetic theory |
| Plant | 1078 | 3100.0 | 0.55 | – | – |
| Lamp | 1380 | 1.3 | 0.20 | – | – |
| Black film | 1400 | 1.3 | 0.20 | – | – |
| Aluminum | 2719 | 871.0 | 202.40 | – | – |

**Table 3.3** Boundary conditions for the case simulation domain.

| Location | Momentum equation | Energy equation | Radiation equation | Species equation |
|---|---|---|---|---|
| Shelf surfaces | No-slip | Convection<br>Heat transfer coefficient ($1.6\ W\ m^{-2}\ K^{-1}$)<br>Free stream temperature (26 °C) | Emissivity (0.10) | Zero diffusive flux |
| Lamp surfaces | No-slip | Wall temperature | Direct irradiation<br>Emissivity (1.00) | Zero diffusive flux |
| Leaf surfaces | No-slip | Coupling<br>Wall thickness (0.001 m)<br>Heat generation rate ($-88209\ W\ m^{-3}$) | Emissivity (0.95) | Water vapor source |
| Inlet | Inlet velocity | Inlet temperature | Emissivity (0.00) | $H_2O$ mole fraction |
| Outlet | Atmospheric pressure | Outlet temperature (25 °C) | Emissivity (1.00) | Zero diffusive flux |

**Table 3.4** Inflow parameters and lamp power of cases.

| Case | $v_{in}$ ($m\ s^{-1}$) | $T_{in}$ (°C) | $RH_{in}$ (%) | $H_2O$ mole fraction | $5P_W$ (W) |
|---|---|---|---|---|---|
| 1 | 0.2 | 23 | 60 | 0.016643 | 159.3 |
| 2 | 0.2 | 23 | 65 | 0.018030 | 159.3 |
| 3 | 0.2 | 23 | 70 | 0.019415 | 159.3 |
| 4 | 0.2 | 24 | 60 | 0.017676 | 159.4 |
| 5 | 0.2 | 24 | 65 | 0.019150 | 159.4 |
| 6 | 0.2 | 24 | 70 | 0.020624 | 159.4 |
| 7 | 0.2 | 25 | 60 | 0.018766 | 159.1 |
| 8 | 0.2 | 25 | 65 | 0.020330 | 159.1 |
| 9 | 0.2 | 25 | 70 | 0.021895 | 159.1 |
| 10 | 0.5 | 23 | 60 | 0.016643 | 159.5 |
| 11 | 0.5 | 23 | 65 | 0.018030 | 159.5 |
| 12 | 0.5 | 23 | 70 | 0.019415 | 159.5 |
| 13 | 0.5 | 24 | 60 | 0.017676 | 159.6 |
| 14 | 0.5 | 24 | 65 | 0.019150 | 159.6 |
| 15 | 0.5 | 24 | 70 | 0.020624 | 159.6 |
| 16 | 0.5 | 25 | 60 | 0.018766 | 159.1 |
| 17 | 0.5 | 25 | 65 | 0.020330 | 159.1 |
| 18 | 0.5 | 25 | 70 | 0.021895 | 159.1 |
| 19 | 0.8 | 23 | 60 | 0.016643 | 159.6 |
| 20 | 0.8 | 23 | 65 | 0.018030 | 159.6 |

| | | | | | |
|---|---|---|---|---|---|
| 21 | 0.8 | 23 | 70 | 0.019415 | 159.6 |
| 22 | 0.8 | 24 | 60 | 0.017676 | 159.4 |
| 23 | 0.8 | 24 | 65 | 0.019150 | 159.4 |
| 24 | 0.8 | 24 | 70 | 0.020624 | 159.4 |
| 25 | 0.8 | 25 | 60 | 0.018766 | 159.2 |
| 26 | 0.8 | 25 | 65 | 0.020330 | 159.2 |
| 27 | 0.8 | 25 | 70 | 0.021895 | 159.3 |

**Table 3.5** Analysis of variance of leaf, lamp temperature, $Q_C/Q_R$.

| $T_{lamp}$ | | | | | |
|---|---|---|---|---|---|
| Source | Coded coefficients | SS | DF | F-value | P-value |
| Model | 38.8900 | 288.2800 | 9 | 93348 | <0.0001 |
| $v_{in}$ | –3.8300 | 264.50 | 1 | 770800 | <0.0001 |
| $T_{in}$ | 0.8333 | 12.50 | 1 | 36429 | <0.0001 |
| $RH_{in}$ | 0.0000 | 0.0000 | 1 | 0.0000 | 1.0000 |
| $v_{in}T_{in}$ | 0.0750 | 0.0675 | 1 | 197 | <0.0001 |
| $v_{in}RH_{in}$ | 0.0000 | 0.0000 | 1 | 0 | 1.0000 |
| $T_{in}RH_{in}$ | 0.0000 | 0.0000 | 1 | 0 | 1.0000 |
| $v_{in}^2$ | 1.3700 | 11.2100 | 1 | 32659 | <0.0001 |
| $T_{in}^2$ | –0.0333 | 0.0067 | 1 | 19 | 0.0004 |
| $RH_{in}^2$ | 0.0000 | 0.0000 | 1 | 0 | 1.0000 |
| Residual | | 0.0058 | 17 | | |
| Total | | 288.2900 | 26 | | |
| $Q_C/Q_R$ | | | | | |
| Source | Coded coefficients | SS | DF | F-value | P-value |
| Model | 0.8780 | 3.6400 | 9 | 575900 | <0.0001 |
| $v_{in}$ | 0.4489 | 3.6300 | 1 | 5169000 | <0.0001 |
| $T_{in}$ | –0.0063 | 0.0007 | 1 | 1034 | <0.0001 |
| $RH_{in}$ | 0.0002 | 0.0000 | 1 | 1 | 0.4574 |
| $v_{in}T_{in}$ | –0.0080 | 0.0008 | 1 | 1106 | <0.0001 |
| $v_{in}RH_{in}$ | 0.0002 | 0.0000 | 1 | 1 | 0.3647 |
| $T_{in}RH_{in}$ | 0.0002 | 0.0000 | 1 | 1 | 0.3647 |
| $v_{in}^2$ | –0.0374 | 0.0084 | 1 | 11961 | <0.0001 |
| $T_{in}^2$ | –0.0010 | 0.0000 | 1 | 8 | 0.0129 |
| $RH_{in}^2$ | 0.0002 | 0.0000 | 1 | 0 | 0.6662 |
| Residual | | 0.0000 | 17 | | |
| Total | | 3.6400 | 26 | | |
| $T_{leaf}$ | | | | | |
| Source | Coded coefficients | SS | DF | F-value | P-value |
| Model | 24.79 | 40.6900 | 9 | 5929 | <0.0001 |
| $v_{in}$ | –1.09 | 21.3400 | 1 | 27989 | <0.0001 |
| $T_{in}$ | 0.9722 | 17.0100 | 1 | 22313 | <0.0001 |

| | | | | | |
|---|---|---|---|---|---|
| $RH_{in}$ | 0.0000 | 0.0000 | 1 | 0 | 1.0000 |
| $v_{in}T_{in}$ | 0.0167 | 0.0033 | 1 | 4 | 0.0519 |
| $v_{in}RH_{in}$ | 0.0000 | 0.0000 | 1 | 0 | 1.0000 |
| $T_{in}RH_{in}$ | 0.0000 | 0.0000 | 1 | 0 | 1.0000 |
| $v_{in}^2$ | 0.6222 | 2.3200 | 1 | 3046 | <0.0001 |
| $T_{in}^2$ | –0.0278 | 0.0046 | 1 | 6 | 0.0247 |
| $RH_{in}^2$ | –0.0111 | 0.0007 | 1 | 1 | 0.3381 |
| Residual | | 0.0130 | 17 | | |
| Total | | 40.7000 | 26 | | |

**Table 3.6** Analysis of variance of unsatisfactory microclimate zones ($V_v$, $V_T$, and $V_{RH}$).

| $V_v$ | | | | | |
|---|---|---|---|---|---|
| Source | Coded coefficients | SS | DF | F-value | P-value |
| Model | 0.0841 | 0.3516 | 9 | 2737000 | <0.0001 |
| $v_{in}$ | –0.1328 | 0.3177 | 1 | 22250000 | <0.0001 |
| $T_{in}$ | 0.0001 | 0.0000 | 1 | 24 | 0.0001 |
| $RH_{in}$ | –0.0000 | 0.0000 | 1 | 0 | 0.9597 |
| $v_{in}T_{in}$ | 0.0000 | 0.0000 | 1 | 0 | 0.6845 |
| $v_{in}RH_{in}$ | 0.0000 | 0.0000 | 1 | 0 | 0.9970 |
| $T_{in}RH_{in}$ | –0.0000 | 0.0000 | 1 | 0 | 0.9890 |
| $v_{in}^2$ | 0.0752 | 0.0339 | 1 | 2376000 | <0.0001 |
| $T_{in}^2$ | –0.0000 | 0.0000 | 1 | 0 | 0.9289 |
| $RH_{in}^2$ | –0.0000 | 0.0000 | 1 | 0 | 0.9882 |
| Residual | | 0.0000 | 17 | | |
| Total | | 0.3516 | 26 | | |
| $V_T$ | | | | | |
| Source | Coded coefficients | SS | DF | F-value | P-value |
| Model | 0.0428 | 0.3054 | 9 | 120 | <0.0001 |
| $v_{in}$ | –0.0289 | 0.0150 | 1 | 53 | <0.0001 |
| $T_{in}$ | 0.1172 | 0.2471 | 1 | 870 | <0.0001 |
| $RH_{in}$ | 0.0000 | 0.0000 | 1 | 0 | 0.9987 |
| $v_{in}T_{in}$ | –0.0092 | 0.0010 | 1 | 4 | 0.0752 |
| $v_{in}RH_{in}$ | 0.0000 | 0.0000 | 1 | 0 | 0.9991 |
| $T_{in}RH_{in}$ | 0.0000 | 0.0000 | 1 | 0 | 0.9997 |
| $v_{in}^2$ | 0.0180 | 0.0019 | 1 | 7 | 0.0182 |
| $T_{in}^2$ | 0.0820 | 0.0404 | 1 | 142 | <0.0001 |
| $RH_{in}^2$ | –0.0000 | 0.0000 | 1 | 0 | 0.9953 |
| Residual | | 0.0048 | 17 | | |
| Total | | 0.3102 | 26 | | |
| $V_{RH}$ | | | | | |
| Source | Coded coefficients | SS | DF | F-value | P-value |
| Model | 0.0148 | 0.0972 | 9 | 80 | <0.0001 |
| $v_{in}$ | 0.0029 | 0.0001 | 1 | 1 | 0.3113 |
| $T_{in}$ | 0.0007 | 0.0000 | 1 | 0 | 0.7914 |
| $RH_{in}$ | 0.0658 | 0.0778 | 1 | 576 | <0.0001 |
| $v_{in}T_{in}$ | 0.0005 | 0.0000 | 1 | 0 | 0.8791 |
| $v_{in}RH_{in}$ | 0.0124 | 0.0018 | 1 | 14 | 0.0018 |

| | | | | | |
|---|---|---|---|---|---|
| $T_{in}RH_{in}$ | 0.0018 | 0.0000 | 1 | 0 | 0.6031 |
| $v_{in}^2$ | –0.0013 | 0.0000 | 1 | 0 | 0.7799 |
| $T_{in}^2$ | –0.0002 | 0.0000 | 1 | 0 | 0.9644 |
| $RH_{in}^2$ | 0.0537 | 0.0173 | 1 | 128 | <0.0001 |
| Residual | | 0.0023 | 17 | | |
| Total | | 0.0995 | 26 | | |

**Table 3.7** Analysis of variance of microclimate uniformity ($CV_v$, $CV_T$, and $CV_{RH}$).

| $CV_v$ | | | | | |
|---|---|---|---|---|---|
| Source | Coded coefficients | SS | DF | F-value | P-value |
| Model | 0.7161 | 0.0257 | 9 | 83180 | <0.0001 |
| $v_{in}$ | –0.0362 | 0.0235 | 1 | 686200 | <0.0001 |
| $T_{in}$ | 0.0007 | 0.0000 | 1 | 233 | <0.0001 |
| $RH_{in}$ | 0.0000 | 0.0000 | 1 | 0 | 1.0000 |
| $v_{in}T_{in}$ | –0.0007 | 0.0000 | 1 | 197 | <0.0001 |
| $v_{in}RH_{in}$ | 0.0000 | 0.0000 | 1 | 0 | 1.0000 |
| $T_{in}RH_{in}$ | 0.0000 | 0.0000 | 1 | 0 | 1.0000 |
| $v_{in}^2$ | 0.0188 | 0.0021 | 1 | 62021 | <0.0001 |
| $T_{in}^2$ | 0.0003 | 0.0000 | 1 | 19 | <0.0500 |
| $RH_{in}^2$ | 0.0000 | 0.0000 | 1 | 1 | 1.0000 |
| Residual | | 0.0000 | 17 | | |
| Total | | 0.0257 | 26 | | |
| $CV_T$ | | | | | |
| Source | Coded coefficients | SS | DF | F-value | P-value |
| Model | 0.1479 | 0.0435 | 9 | 31801 | <0.0001 |
| $v_{in}$ | –0.0473 | 0.0403 | 1 | 265400 | <0.0001 |
| $T_{in}$ | –0.0075 | 0.0010 | 1 | 6663 | <0.0001 |
| $RH_{in}$ | 0.0000 | 0.0000 | 1 | 0 | 1.0000 |
| $v_{in}T_{in}$ | 0.0023 | 0.0001 | 1 | 400 | <0.0001 |
| $v_{in}RH_{in}$ | 0.0000 | 0.0000 | 1 | 0 | 1.0000 |
| $T_{in}RH_{in}$ | 0.0000 | 0.0000 | 1 | 0 | 1.0000 |
| $v_{in}^2$ | 0.0187 | 0.0021 | 1 | 13758 | <0.0001 |
| $T_{in}^2$ | 0.0002 | 0.0000 | 1 | 1 | 0.3096 |
| $RH_{in}^2$ | 0.0000 | 0.0000 | 1 | 0 | 1.0000 |
| Residual | | 0.0000 | 17 | | |
| Total | | 0.0435 | 26 | | |
| $CV_{RH}$ | | | | | |
| Source | Coded coefficients | SS | DF | F-value | P-value |
| Model | 0.1981 | 0.0930 | 9 | 33623 | <0.0001 |
| $v_{in}$ | –0.0699 | 0.0879 | 1 | 286200 | <0.0001 |
| $T_{in}$ | –0.0042 | 0.0003 | 1 | 1018 | <0.0001 |
| $RH_{in}$ | –0.0031 | 0.0002 | 1 | 567 | <0.0001 |
| $v_{in}T_{in}$ | 0.0017 | 0.0000 | 1 | 109 | <0.0001 |

| | | | | | |
|---|---|---|---|---|---|
| $v_{in}RH_{in}$ | 0.0017 | 0.0000 | 1 | 109 | <0.0001 |
| $T_{in}RH_{in}$ | 0.0002 | 0.0000 | 1 | 1 | 0.3121 |
| $v_{in}^2$ | 0.0273 | 0.0045 | 1 | 14593 | <0.0001 |
| $T_{in}^2$ | –0.0002 | 0.0000 | 1 | 1 | 0.4714 |
| $RH_{in}^2$ | 0.0003 | 0.0000 | 1 | 2 | 0.1590 |
| Residual | | 0.0000 | 17 | | |
| Total | | 0.0930 | 26 | | |

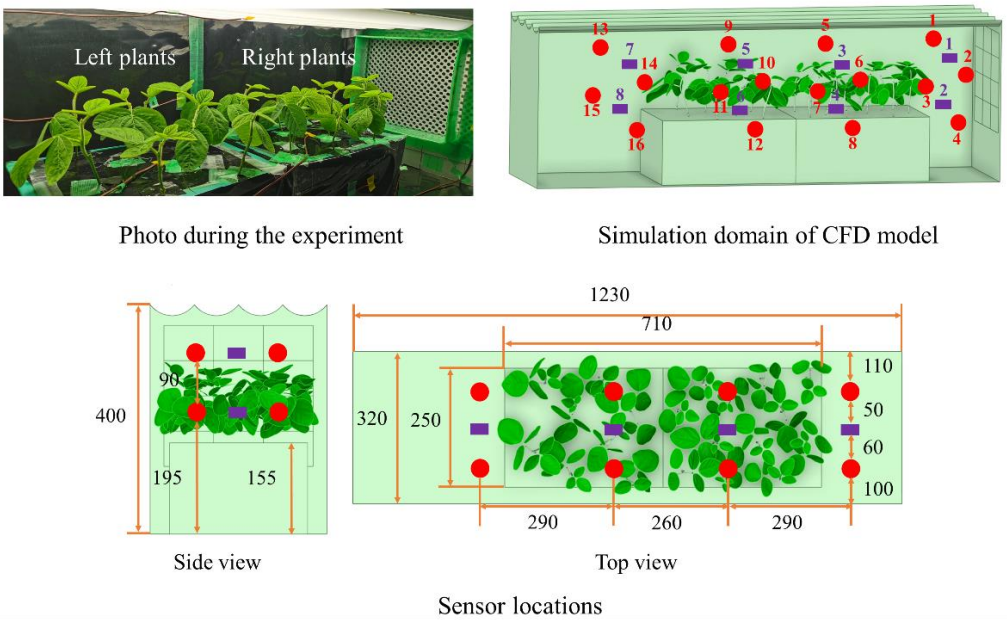


**Figure 3.1** Experimental setup and sensor locations. The red measured points (No. 1–16) were for verifying air velocity and temperature. The purple measured points (No. 1–8) were for verifying relative humidity. Unit: mm. The front panel has been removed for photography. The two hydroponics containers were located in the shelf. The right containers plants have smaller leaf area compared to that of left one.

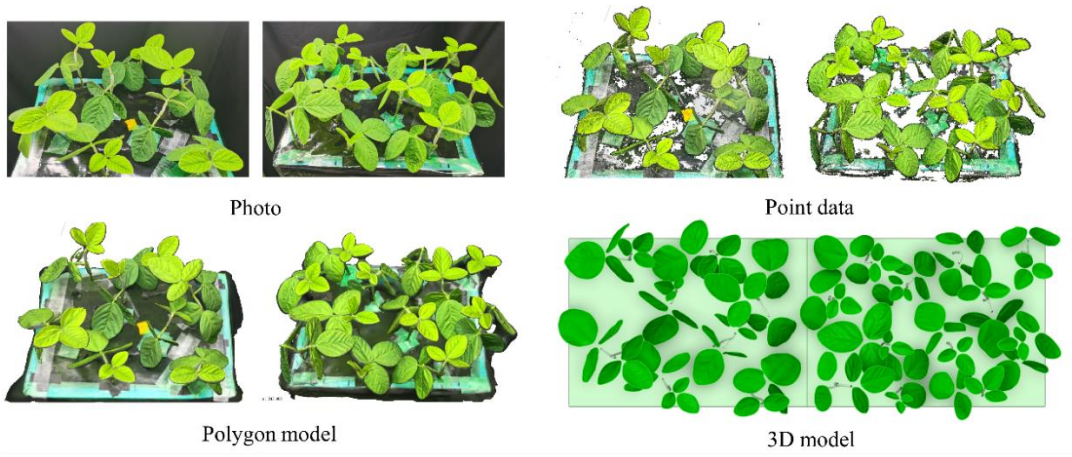


**Figure 3.2** Procedure of 3D modeling of soybean canopies. The two hydroponics containers were located in the shelf (Figure 3.1). The right containers plants have smaller leaf area compared to that of left one.

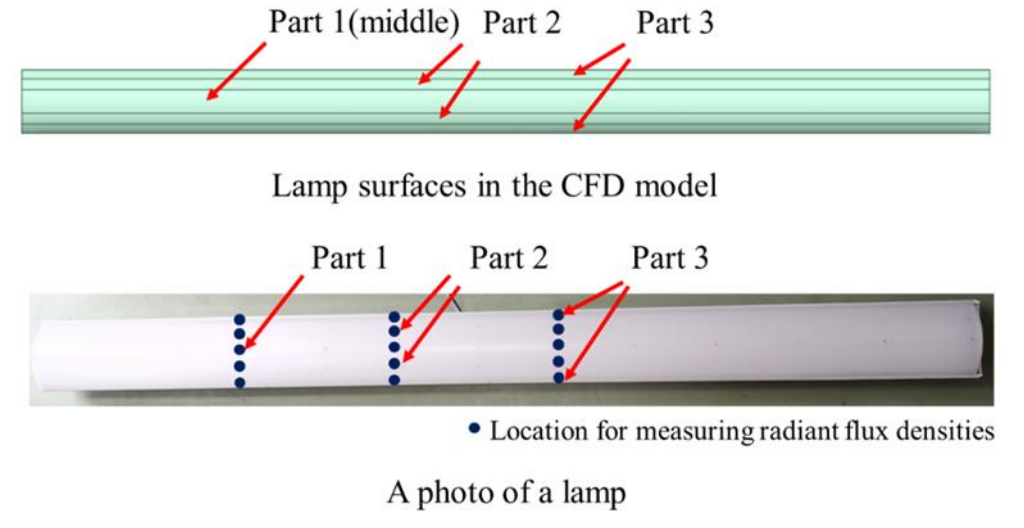


**Figure 3.3** Lamp surfaces in CFD model and a lamp photo. The PAR flux transmitted through the lamp surface was uneven. The radiation intensity in the middle (Part 1) was higher than that on both sides (Parts 2 and 3). Therefore, the lamp surface was divided into three parts to set boundary conditions for the radiation equation.

**Figure 3.4** A photo of measuring transpiration rate under different inflow parameters (velocities: 0.2–0.8 m $s^{-1}$; temperatures: 23–25 °C; and humidities: 60–70%). The deviation of transpiration was smaller than 6.5% under those conditions.

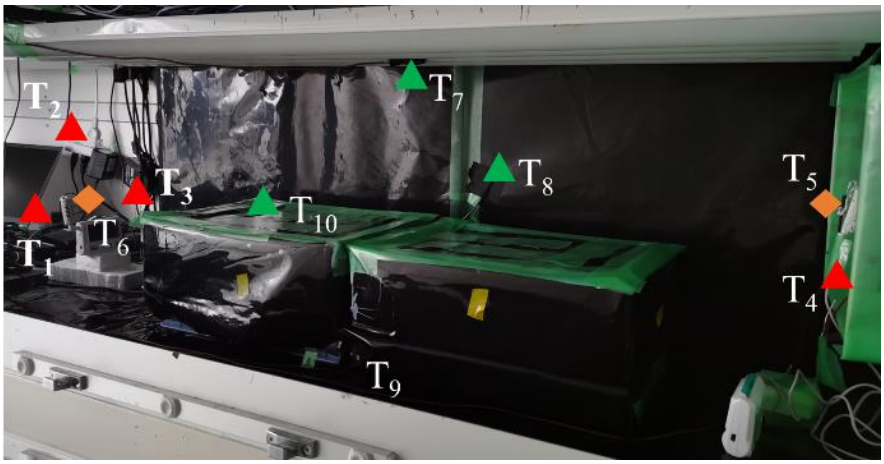


**Figure 3.5** Experimental measurements for air exchange model. $T_1$–$T_3$ are for measuring outlet air temperature; $T_4$ is for measuring inlet air temperature; $T_5$ and $T_6$ are for measuring inlet and outlet relative humidity, respectively; $T_7$–$T_{10}$ are for measuring wall temperatures. The front panel is removed for photography.

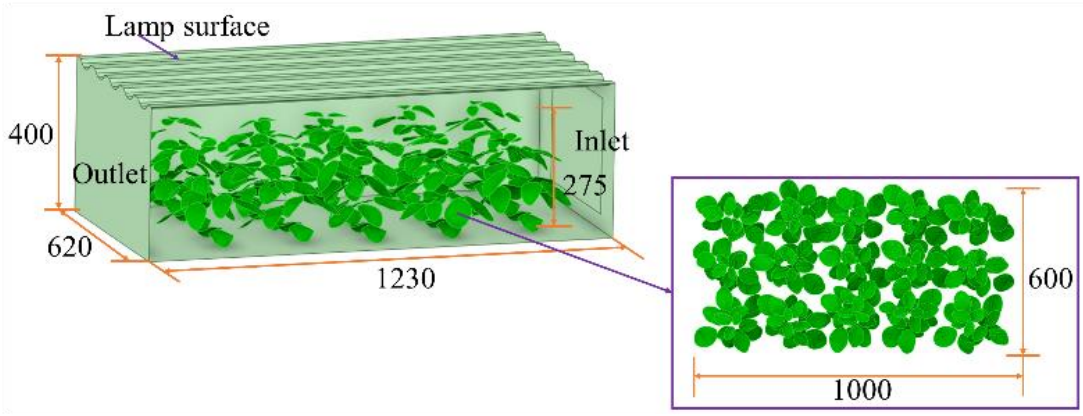


**Figure 3.6** Simulation domain of cases. Unit: mm.

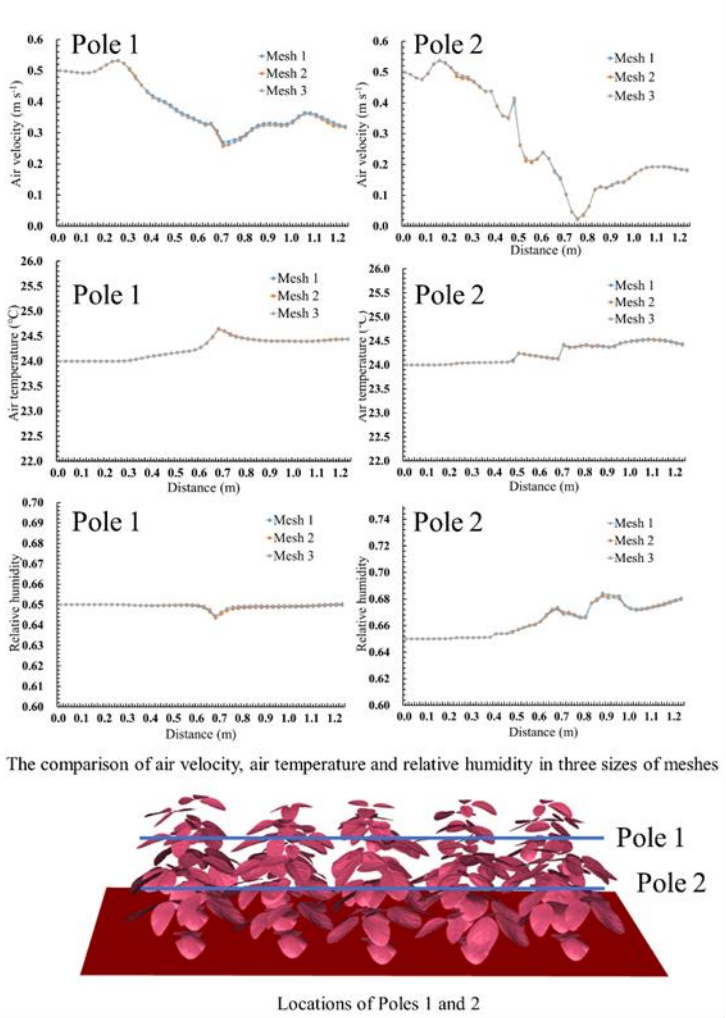


**Figure 3.7** Mesh independence test. Three sizes of meshes (Mesh 1: 1.3 million; Mesh 2: 2.3 million; Mesh 3: 4.5 million) were compared with the axial air velocity, air

temperature, and relative humidity profiles along the shelf length at two poles.

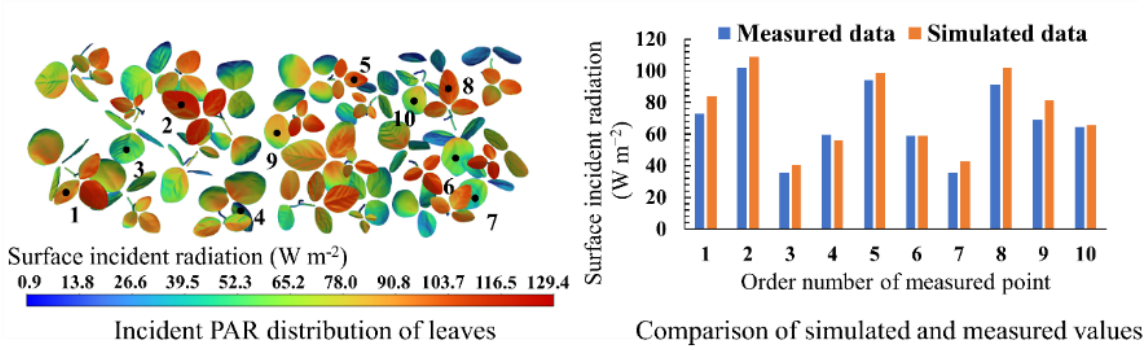


**Figure 3.8** Simulated PAR validation. The numbers on the contour of leaf surface light radiation correspond to the order number of measured points.

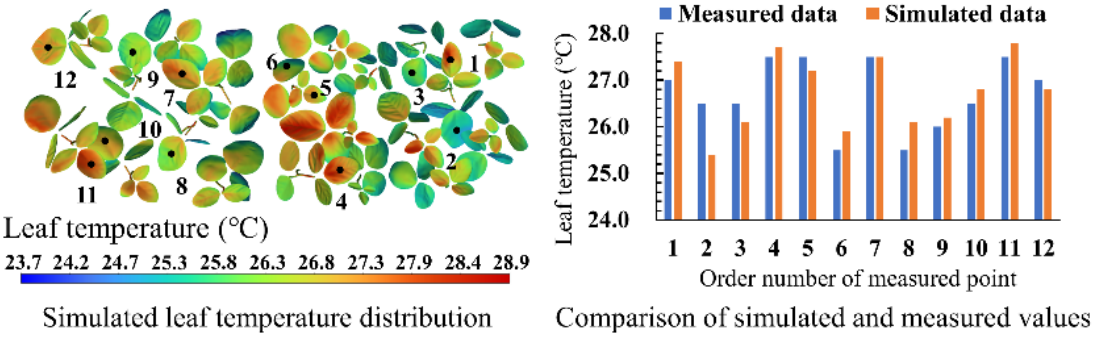


**Figure 3.9** Simulated leaf temperature validation. The numbers on the contour of leaf temperature correspond to the order number of measured points.

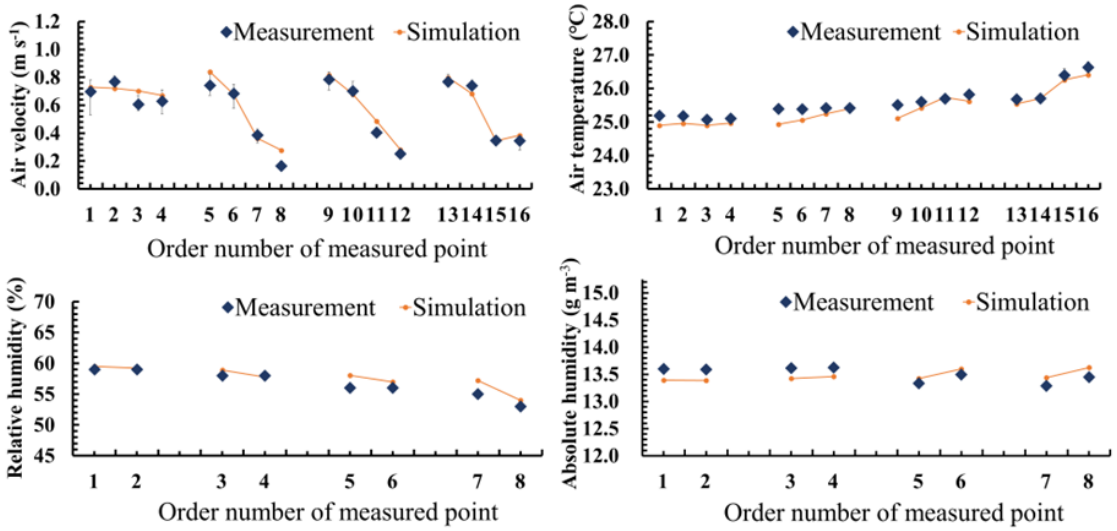


**Figure 3.10** Validation of simulated air velocity, air temperature, relative humidity and absolute humidity. The error bar shows measured mean values and observed minimum and maximum values during a measurement period.

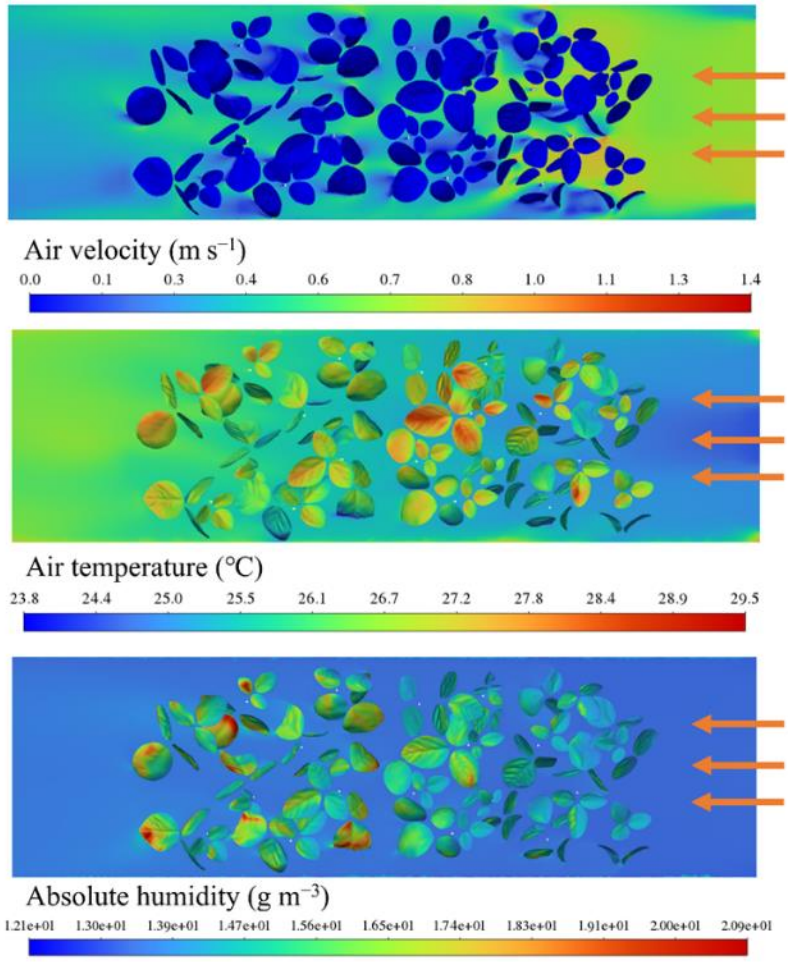


**Figure 3.11** Calculated air velocity, air temperature and absolute humidity at a plane located at the mid-height of the plant canopy.

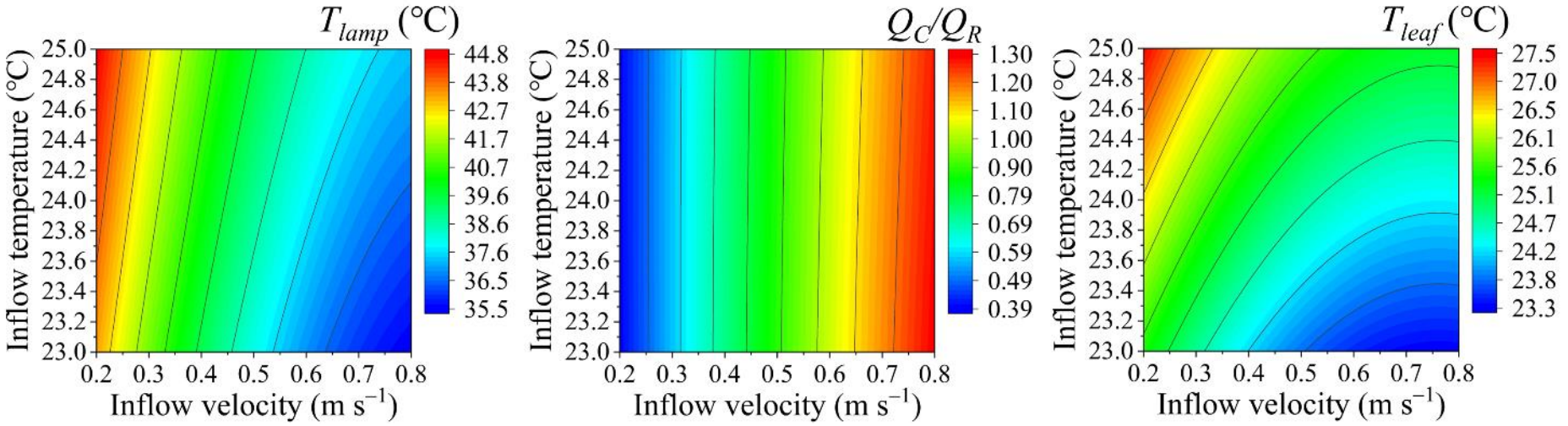


**Figure 3.12** Contour plots of lamp temperature ($T_{lamp}$), $Q_C/Q_R$, and leaf temperature ($T_{leaf}$) in relation to inflow velocity ($v_{in}$) and inflow temperature ($T_{in}$).

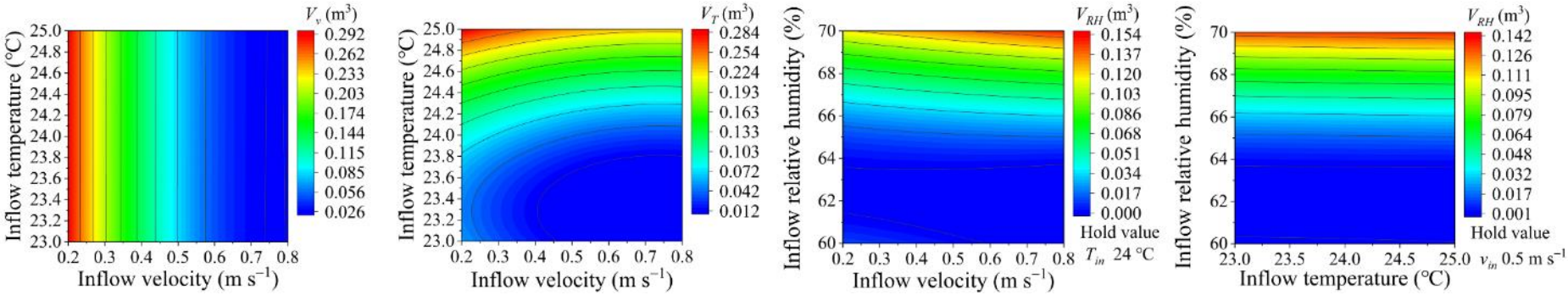


**Figure 3.13** Contour plots of the volumes of zones where air velocity <0.2 m $s^{-1}$ ($V_v$) and air temperature >25 °C ($V_T$) in relation to inflow velocity ($v_{in}$) and temperature ($T_{in}$), and the volumes of zones where relative humidity >70% ($V_{RH}$) in relation to inflow relative humidity ($RH_{in}$) and air velocity ($v_{in}$) with a 24 °C inflow temperature and inflow relative humidity ($RH_{in}$) and temperature ($T_{in}$) with a 0.5 m $s^{-1}$ inflow velocity.

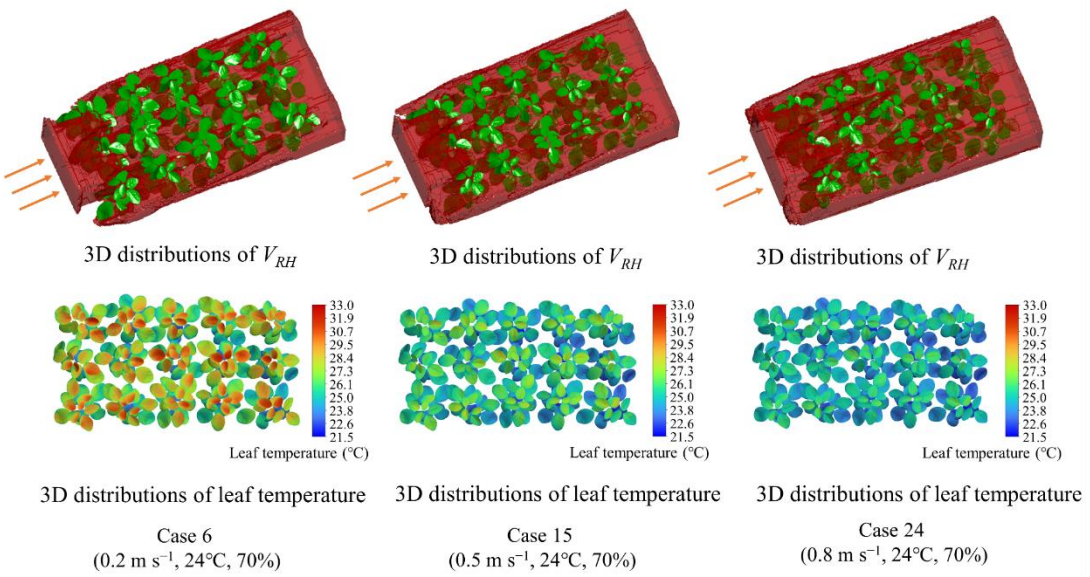


**Figure 3.14** $V_{RH}$ and leaf temperature of 3D distributions for cases 6, 15, and 24. Red zones in the top images indicate high relative humidity (>70%).

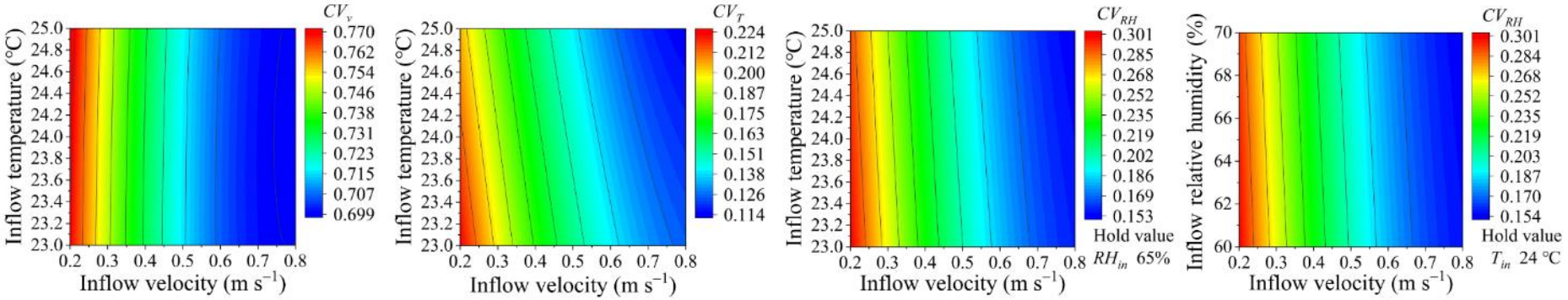


**Figure 3.15** Contour plots of the coefficient of variation (CV) of air velocity ($CV_v$) and air temperature ($CV_T$) in relation to inflow velocity ($v_{in}$) and temperature ($T_{in}$), and the *CV* of air relative humidity ($CV_{RH}$) in relation to inflow temperature ($T_{in}$) and velocity ($v_{in}$) with a 65% inflow relative humidity ($RH_{in}$) and inflow relative humidity ($RH_{in}$) and air velocity ($v_{in}$) with a 24 °C inflow temperature.

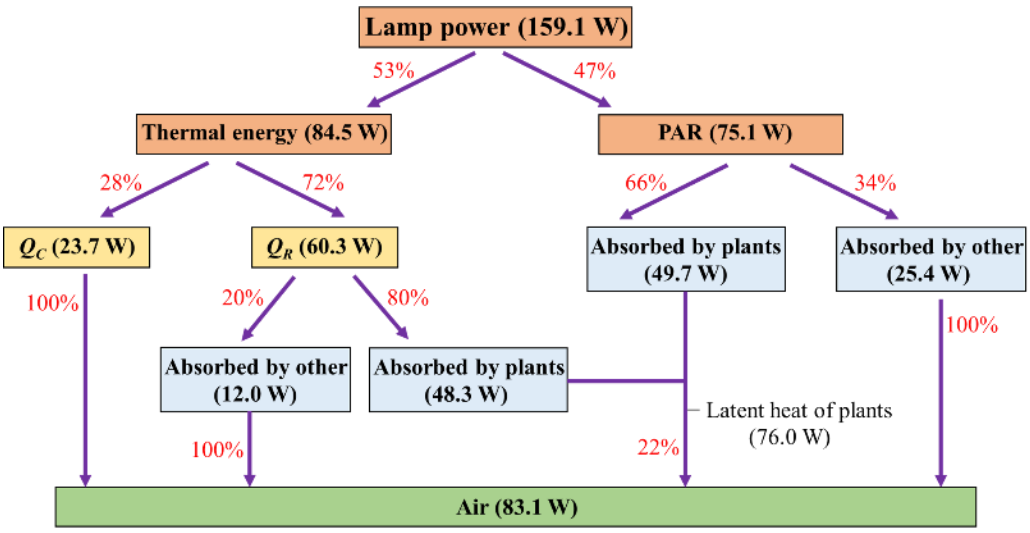


**Figure 3.16** Energy transfer between lamps and air in Case 8.

# CHAPTER 4.

# Conclusions

## 4.1. Summary

This dissertation aimed to develop a CFD model with realistic plants evaluating plant canopy microclimate and transpiration in a shelf of a PFAL to provide a strategy for designing airflow control to improve plant growth and development.

In Chapter 2, a CFD model with realistic plant structures was developed to study the airflow in and around a plant canopy. Realistic plant structures were established using structure-from-motion imaging. The effects of inflow velocity and plant canopy structure on airflow are summarized as follows: A high inflow velocity significantly improved airflow and uniformity in the plant canopy. The staggered layout of the plant canopy slightly enhanced the air velocity and uniformity in and around the plant canopy. With plant growth, the airflow in and around the plant canopy was hindered; however, the air velocity around the partial leaves increased. Leaf veins have unfavorable effects on air velocity on leaf surfaces, decreasing the uniformity of airflow in and around the plant canopy. The stagnant zones on the windward side of the plants were difficult to eliminate even at a high inflow velocity.

In Chapter 3, a CFD model with realistic plant structures integrated into the lamp energy model was developed to quantitatively analyze the spatial microclimate under different inflow parameters in a shelf of PFALs. Results showed that inflow velocity and temperature significantly affected lamp temperature, the ratio of convective heat transfer energy to the thermal radiation of lamps, and leaf temperature. Inflow velocity, temperature, and relative humidity exerted more significant effects on air velocity, temperature, and humidity, respectively, than other variables did in the plant canopy. Inflow velocity significantly improved the uniformity of air velocity, temperature, and humidity in the plant canopy. At lamp and canopy locations, different airflow control

methods were recommended to be considered. The most optimal inflow parameters for this study were identified as 0.8 m $s^{-1}$, 24 °C, and 65% relative humidity.

## 4.2. Suggestions for future research

The present CFD model with realistic plants allows quantitative and visual assessment of the microclimate in and around a plant canopy under different inflow controls and plant structures. The results provide a foundational understanding for optimizing the microclimate in and around the plant canopy. It offers insights for designing more efficient airflow control in a closed-type cultivation shelf of PFALs. However, there are some limitations.

In contrast to the widely adopted ray-tracing method for light environment simulations (Kim et al., 2020), the Discrete Ordinates (DO) model discretizes directions in space to solve radiative transfer. Notably, it demonstrates the capability to simulate radiation transfer in current 3D plant canopies while also significantly reducing computation time. However, challenges arise when utilizing the 0-thickness leaf model for simulating radiation transmission through leaves with the DO model. Despite lower radiation transmittance compared to absorptance in leaves, exploring alternative methods becomes necessary for further enhancement.

The transpiration model significantly affects the accuracy of the CFD model. However, transpiration is a very complex phenomenon in which plants interact with microclimate. Future studies are expected to develop a high precise transpiration model and its integration into existing CFD models to further enhance their applicability.

In addition, the transpiration rate of plant canopies was influenced not only by the intensity of air temperature, radiation, air velocity, and VPD but also by the fluctuation parameters of these variables. Further studies are anticipated to explore the relationship between the physiological activities, growth and development, yield of plants, and environmental factor fluctuations to provide valuable theoretical insights for optimizing airflow control strategies.

Chapters 2 and 3 centered on inflow control strategies aimed at optimizing the microclimate of plant canopies. However, further research is needed to explore additional methods for enhancing airflow control within cultivation shelves. Therefore, future studies are projected to utilize the current CFD model to simulate the distribution of plant canopy microclimate and transpiration under various airflow control scenarios. Through this process, the most effective airflow control strategy will be identified and implemented to maximize plant growth and productivity.

## REFERENCES


Agati, G., Franchetti, B., Rispoli, F., Venturini, P., 2024. Thermo-fluid dynamic analysis of the air flow inside an indoor vertical farming system. Appl. Therm. Eng. 236, 121553. https://doi.org/10.1016/j.applthermaleng.2023.121553

Ahmed, H.A., Tong, Y.X., Yang, Q.C., 2020. Lettuce plant growth and tipburn occurrence as affected by airflow using a multi-fan system in a plant factory with artificial light. J. Therm. Biol. 88, 102496. https://doi.org/10.1016/j.jtherbio.2019.102496

Allen, R.G., Smith, M., Pereira, L.S., Perrier, A., 1994. An update for the calculation of reference evapotranspiration. ICID Bull. 43, 35–92.

Baek, M.S., Kwon, S.Y., Lim, J.H., 2016. Improvement of the crop growth rate in plant factory by promoting air flow inside the cultivation. Int. J. Smart Home 10, 63–74. http://doi.org/10.14257/ijsh.2016.10.2.07

Bartzanas, T., Kacira, M., Zhu, H., Karmakar, S., Tamimi, E., Katsoulas, N., Lee, I.B., Kittas, C., 2013. Computational fluid dynamics applications to improve crop production systems. Comput. Electron. Agric. 93, 151–167. https://doi.org/10.1016/j.compag.2012.05.012

Bouhoun Ali, H., Bournet, P.E., Cannavo, P., Chantoiseau, E., 2018. Development of a CFD crop submodel for simulating microclimate and transpiration of ornamental plants grown in a greenhouse under water restriction. Comput. Electron. Agric. 149, 26–40. https://doi.org/10.1016/j.compag.2017.06.021

Boulard, T., Roy, J.C., Pouillard, J.B., Fatnassi, H., Grisey, A., 2017. Modelling of micrometeorology, canopy transpiration and photosynthesis in a closed greenhouse using computational fluid dynamics. Biosyst. Eng. 158, 110–133. http://doi.org/10.1016/j.biosystemseng.2017.04.001

Boulard, T., Wang, S., 2002. Experimental and numerical studies on the heterogeneity of crop transpiration in a plastic tunnel. Comput. Electron. Agric. 34, 173–190. http://dx.doi.org/10.1016/S0168-1699(01)00186-7.

Bournet, P.E., Ould Khaoua, S.A., Boulard, T., 2007. Numerical prediction of the effect of vent arrangements on the ventilation and energy transfer in a multi-span glasshouse using a bi-band radiation model. Biosyst. Eng. 98, 224–234. https://doi.org/10.1016/j.biosystemseng.2007.06.007

Chen, H.Y., Chen, C., 2016. Determining the emissivity and temperature of building materials by infrared thermometer. Constr. Build. Mater. 126, 130–137.

Chen, L., Zhang, M., Li, D., Li, Y., 2023. Infrared thermographic evaluation of thermal release phenomena in polycarbonate during plastic deformation. Adv. Ind. Eng. Polym. Res. 6, 39–48. https://doi.org/10.1016/j.aiepr.2022.10.002.

de Vries, D.A., 1963. The physics of plant environments. In L.T. Evans (Eds.), Environmental Control of Plant Growth, Academic press Inc., New York, pp. 5–21.

Duga, A.T., Dekeyser, D., Ruysen, K., Bylemans, D., Nuyttens, D., Nicolai, B.M., Verboven, P., 2015. Numerical analysis of the effects of wind and sprayer type on spray distribution in different orchard training systems. Boundary-Layer Meteorol. 157, 517–535. https://doi.org/10.1007/s10546-015-0064-2

Endalew, A.M., Hertog, M., Delele, M.A., Baetens, K., Persoons, T., Baelmans, M., Ramon, H., Nicolaï, B.M., Verboven, P., 2009. CFD modelling and wind tunnel validation of airflow through plant canopies using 3D canopy architecture. Int. J. Heat Fluid Flow 30, 356–368. https://doi.org/10.1016/j.ijheatfluidflow.2008.12.007

Fang, H., Li, K., Wu, G., Cheng, R., Zhang, Y., Yang, Q.C., 2020. A CFD analysis on improving lettuce canopy airflow distribution in a plant factory considering the crop resistance and LEDs heat dissipation. Biosyst. Eng. 200, 1–12. https://doi.org/10.1016/j.biosystemseng.2020.08.017

Fatnassi, H., Boulard, T., Poncet, C., Chave, M., 2006. Optimisation of greenhouse insect screening with computational fluid dynamics. Biosys. Eng. 93, 301–312. http://dx.doi.org/10.1016/j.biosystemseng.2005.11.014.

Fluent User's guide, 2021 version 2021 R2. ANSYS Inc.

Goto, E., 2012. Plant production in a closed plant factory with artificial lighting. Acta Hortic. 956, 37–49. https://doi.org/10.17660/ActaHortic.2012.956.2

Goto, E., Ishigami, Y., Kimura, K., Arai, K., Kashima, K., Nakajima, H., Maruyama, S., 2014. Optimum air current speed for rice plant canopy in a closed plant production system. Acta Hortic. 1037, 305–310. https://doi.org/10.17660/ActaHortic.2014.1037.36

Goto, E., Takakura, T., 1992. Prevention of lettuce tipburn by supplying air to inner leaves. Trans. Am. Soc. Agric. Eng. 35, 641–645. https://doi.org/10.13031/2013.28644

Gromke, C., Blocken, B., Janssen, W., Merema, B., van Hooff, T., Timmermans, H., 2015. CFD analysis of transpirational cooling by vegetation: Case study for specific meteorological conditions during a heat wave in Arnhem, Netherlands, Build. Environ. 83, 11–26. https://doi.org/10.1016/j.buildenv.2014.04.022.

Guo, Z., Yang, X., Wu, X., Zou, X., Zhang, C., Fang, H., Xiang, H., 2021. Optimal design for vegetative windbreaks using 3D numerical simulations. Agric. For. Meteorol. 298–299, 108290. https://doi.org/10.1016/j.agrformet.2020.108290

Haibo, Y., Lei, Z., Haiye, Y., Yucheng, L., Chunhui, L., Yuanyuan, S., 2023. Sustainable development optimization of a plant factory for reducing tip burn disease. Sustainability 15, 5607. https://doi.org/10.3390/su15065607

Hong, S.W., Zhao, L., Zhu, H., 2018. CFD simulation of pesticide spray from air-assisted sprayers in an apple orchard: Tree deposition and off-target losses. Atmos. Environ. 175, 109–119. https://doi.org/10.1016/j.atmosenv.2017.12.001

Hou, M., Tian, F., Zhang, T., Huang, M., 2019. Evaluation of canopy temperature depression, transpiration, and canopy greenness in relation to yield of soybean at reproductive stage based on remote sensing imagery, Agric. Water Manag. 222, 182–192. https://doi.org/10.1016/j.agwat.2019.06.005.

Jay, S., Rabatel, G., Hadoux, X., Moura, D., Gorretta, N., 2015. In-field crop row phenotyping from 3D modeling performed using Structure from Motion. Comput. Electron. Agric. 110, 70–77. https://doi.org/10.1016/j.compag.2014.09.021

Jumrani, K., Bhatia, V. S., Pandey, G. P., 2017. Impact of elevated temperatures on specific leaf weight, stomatal density, photosynthesis and chlorophyll fluorescence in soybean. Photosynth. Res. 131(3), 333-350.

Kang, L., van Hooff, T., 2024. Numerical evaluation and optimization of air distribution system in a small vertical farm with lateral air supply. Dev. Built Environ. 17, 100304. https://doi.org/10.1016/j.dibe.2023.100304

Kim, D., Kang, W.H., Hwang, I., Kim, J., Kim, J.H., Park, K.S., Son, J.E., 2020. Use of structurally-accurate 3D plant models for estimating light interception and photosynthesis of sweet pepper (Capsicum annuum) plants. Comput. Electron. Agric. 177, 105689. https://doi.org/10.1016/j.compag.2020.105689

Kim, Y.H., Kozai, T., Kubota, C., Kitaya, Y., 1996. Effects of air current speeds on the microclimate of plug stand under artificial lighting. Acta Hortic. https://doi.org/10.17660/ActaHortic.1996.440.62

Kitaya, Y., 2005. Importance of air movement for promoting gas and heat exchanges between plants and atmosphere under controlled environments. In K. Omasa, I. Nouchi and L. J. De Kok (Eds.), Plant responses to air pollution and global change, Springer, Luxembourg, pp. 185–193.

Kitaya, Y., Shibuya, T., Kozai, T., Kubota, C., 1998. Effects of light intensity and air velocity on air temperature, water vapor pressure, and $CO_2$ concentration inside a plant canopy under an artificial lighting condition. Life Support Biosph. Sci. 5, 199–203.

Kitaya, Y., Shibuya, T., Yoshida, M., Kiyota, M., 2004. Effects of air velocity on photosynthesis of plant canopies under elevated $CO_2$ levels in a plant culture system. Adv. Sp. Res. 34, 1466–1469. https://doi.org/10.1016/j.asr.2003.08.031

Korthals, R.L., Knight, S.L., Christianson, L.L., Spomer, L.A., 1994. Chambers for studying the effects of airflow velocity on plant growth. Biotronics 23, 113–119.

Kozai, T., 2013a. Plant factory in Japan: current situation and perspectives. Chron. Horticult. 53, 8–11.

Kozai, T., 2013b. Sustainable plant factory: Closed plant production systems with

artificial light for high resource use efficiencies and quality produce. Acta Hortic. 1004, 27–40. https://doi.org/10.17660/ActaHortic.2013.1004.2

Kozai, T., Chun, C., Ohyama, K., 2004. Closed systems with lamps for commercial production of transplants using minimal resources. Acta Hortic. 630, 239–252. https://doi.org/10.17660/ActaHortic.2004.630.30

Kozai, T., Niu, G., 2019. Plant factory: an indoor vertical farming system for efficient quality food production: second edition. Elsevier, Amsterdam, pp. 3.

Lee, S.W., Seo, I.H., An, S.W., Na, H.Y., 2023. Improvement of environmental uniformity in a seedling plant factory with porous panels using computational fluid dynamics. Horticulturae 9, 1027. https://doi.org/10.3390/horticulturae9091027

Liebman-Pelaez, M., Kongoletos, J., Norford, L.K., Reinhart, C., 2021. Validation of a building energy model of a hydroponic container farm and its application in urban design. Energy Build. 250, 111192. https://doi.org/10.1016/j.enbuild.2021.111192

Lim, T.G., Kim, Y.H., 2014. Analysis of airflow pattern in plant factory with different inlet and outlet locations using computational fluid dynamics. J. Biosyst. Eng. 39, 310–317. https://doi.org/10.5307/jbe.2014.39.4.310

Liu, C., Zheng, Z., Cheng, H., Zou, X., 2018. Airflow around single and multiple plants. Agric. For. Meteorol. 252, 27–38. https://doi.org/10.1016/j.agrformet.2018.01.009

Liu, Q., Ke, X., Yoshida, H., Hikosaka, S., Goto, E., 2024. Optimizing photosynthetic photon flux density and light quality for maximizing space use efficacy in edamame at the vegetative growth stage. Front. Sustain. Food Syst. 8, 1407359.

Liu, R., Zhang, J., Yang, X., Liu, S., Kang, L., 2021. Simulating Airflow Around Flexible Vegetative Windbreaks. J. Geophys. Res. Atmos. 126, 1–19. https://doi.org/10.1029/2021JD034578

Majdoubi, H., Boulard, T., Fatnassi, H., Bouirden, L., 2009. Airflow and microclimate patterns in a one-hectare Canary type greenhouse: an experimental and CFD assisted study. Agric. For. Meteorol. 149, 1050–1062. http://dx.doi.org/10.1016/j.agrformet.2009.01.002.

Monteith, J. L., Unsworth, M. H., 2013. Principles of environmental physics (4th ed),

Elsevier, Amsterdam, pp. 137–141.

Moriondo, M., Leolini, L., Staglianò, N., Argenti, G., Trombi, G., Brilli, L., Dibari, C., Leolini, C., Bindi, M., 2016. Use of digital images to disclose canopy architecture in olive tree. Sci. Hortic. 209, 1–13. https://doi.org/10.1016/j.scienta.2016.05.021

Naranjani, B., Najafianashrafi, Z., Pascual, C., Agulto, I., Chuang, P.Y.A., 2022. Computational analysis of the environment in an indoor vertical farming system. Int. J. Heat Mass Transf. 186, 122460. https://doi.org/10.1016/j.ijheatmasstransfer.2021.122460

Nebbali, R., Roy, J.C., Boulard, T., 2012. Dynamic simulation of the distributed radiative and convective climate within a cropped greenhouse. Renew. Energy 43, 111–129. https://doi.org/10.1016/j.renene.2011.12.003

Niam, A.G., Muharam, T.R., Widodo, S., Solahudin, M., Sucahyo, L., 2019. CFD simulation approach in determining air conditioners position in the mini plant factory for shallot seed production. In AIP Conference Proceedings. https://doi.org/10.1063/1.5086564

Ohashi, Y., Torii, T., Ishigami, Y., Goto, E., 2020. Estimation of the light interception of a cultivated tomato crop canopy under different furrow distances in a greenhouse using the ray tracing. J. Agric. Meteorol. 76, 188–193. https://doi.org/10.2480/agrmet.D-20-00030

Okayama, T., Okamura, K., Park, J.E., Ushada, M., Murase, H., 2008. A simulation for precision airflow control using multi-fan in a plant factory. Environ. Control Biol. 46, 183–194. https://doi.org/10.2525/ecb.46.183

Pappa, V., Bouris, D., Theurer, W., Gromke, C., 2023. A wind tunnel study of aerodynamic effects of façade and roof greening on air exchange from a cubic building. Build. Environ. 231, 110023. https://doi.org/10.1016/j.buildenv.2023.110023.

Rosenberg, N.J., Blad, B.L., Verma, S.B., 1983. Microclimate: the biological environment. John Wiley & Sons, California. pp. 209–288.

Roy, J.C., Vidal, C., Fargues, J., Boulard, T., 2008. CFD based determination of

temperature and humidity at leaf surface. Comput. Electron. Agric. 61, 201–212. https://doi.org/10.1016/j.compag.2007.11.007

Saito, K., Ishigami, Y., Goto, E., 2020. Evaluation of the light environment of a plant factory with artificial light by using an optical simulation. Agronomy 10, 1663. https://doi.org/10.3390/agronomy10111663

Shibuya, T., Tsuruyama, J., Kitaya, Y., Kiyota, M., 2006. Enhancement of photosynthesis and growth of tomato seedlings by forced ventilation within the canopy. Sci. Hortic. 109, 218–222. https://doi.org/10.1016/j.scienta.2006.04.009

Sohn, J., Liulys, M., Avgoustaki, D.D., Xydis, G., 2023. CFD analysis of airflow uniformity in a Shipping-Container vertical farm. Comput. Electron. Agric. 215, 108363. https://doi.org/10.1016/j.compag.2023.108363

Stanghellini, C., 1987. Transpiration of greenhouse crops: an aid to climate management. IMAG, Wageningen (Thesis).

Stanghellini, C., Ooster, B.V., Heuvelink, E., 2019. Greenhouse horticulture: Technology for optimal crop production. Wageningen Academic Publishers, Wageningen, Netherlands, pp.52.

Su, J., Wang, L., Gu, Z., Song, M., Cao, Z., 2019. Effects of real trees and their structure on pollutant dispersion and flow field in an idealized street canyon. Atmos. Pollut. Res. 10, 1699–1710. https://doi.org/10.1016/j.apr.2019.07.001

Thimijan, R.W., Heins, R.D., 1983. Photometric, radiometric, and quantum light units of measure, a review of procedures for interconversion, J. Am. Soc. Hortic. Sci. 18, 818–822.

Wang, H. W., 2020. Fluid mechanics as I understand it (2nd ed), National Defense Industry Press, Beijing, pp. 130–151.

Wang, H., Zhai, Z.J., 2012. Analyzing grid independency and numerical viscosity of computational fluid dynamics for indoor environment applications. Build. Environ. 52, 107–118. https://doi.org/10.1016/j.buildenv.2011.12.019

Wang, K. C., 2018. Food safety and contract edamame: the geopolitics of the vegetable trade in East Asia. Geogr. Rev. 108, 274–295. https://doi.org/10.1111/gere.12254

Wang, L., Iddio, E., Ewers, B., 2021. Introductory overview: Evapotranspiration (ET) models for controlled environment agriculture (CEA). Comput. Electron. Agric. 190, 106447. https://doi.org/10.1016/j.compag.2021.106447

Yokoi, S., Goto, E., Kozai, T., Nishimura, M., Taguchi, K., Ishigami, Y., 2008. Effects of planting density and air current speed on the growth and uniformity of qing-geng-cai and Spinach plug seedlings in a closed transplant production system. Environ. Control Biol. 46, 103–114. https://doi.org/10.2525/ecb.46.103

Yu, G., Zhang, S., Li, S., Zhang, M., Benli, H., Wang, Y., 2023a. Numerical investigation for effects of natural light and ventilation on 3D tomato body heat distribution in a Venlo greenhouse. Inf. Process. Agric. 10, 535–546. https://doi.org/10.1016/j.inpa.2022.05.006

Yu, H., Yu, H., Zhang, B., Chen, M., Liu, Y., Sui, Y., 2023b. Quantitative perturbation analysis of plant factory led heat dissipation on crop microclimate. Horticulturae 9, 1–16. https://doi.org/10.3390/horticulturae9060660

Zhang, G., Choi, C., Bartzanas, T., Lee, I.B., Kacira, M., 2018. Computational Fluid Dynamics (CFD) research and application in Agricultural and Biological Engineering. Comput. Electron. Agric. 149, 1–2. https://doi.org/10.1016/j.compag.2018.04.007

Zhang, L., Lemeur, R., 1992. Effect of aerodynamic resistance on energy balance and Penman-Monteith estimates of evapotranspiration in greenhouse conditions. Agric. For. Meteorol. 58, 209–228. https://doi.org/10.1016/0168-1923(92)90062-9

Zhang, Y., Kacira, M., 2022. Analysis of climate uniformity in indoor plant factory system with computational fluid dynamics (CFD). Biosyst. Eng. 220, 73–86. https://doi.org/10.1016/j.biosystemseng.2022.05.009

Zhang, Y, Kacira, M., An, L., 2016. A CFD study on improving air flow uniformity in indoor plant factory system. Biosyst. Eng. 147, 193–205. https://doi.org/10.1016/j.biosystemseng.2016.04.012

Zhang, Y., Yasutake, D., Hidaka, K., Kitano, M., Okayasu, T., 2020. CFD analysis for evaluating and optimizing spatial distribution of $CO_2$ concentration in a strawberry

greenhouse under different $CO_2$ enrichment methods. Comput. Electron. Agric. 179, 105811. https://doi.org/10.1016/j.compag.2020.105811

## ACKNOWLEDGEMENTS

I would like to extend my heartfelt gratitude and respect to everyone who has played a role in my Ph.D. research.

First and foremost, I want to express my deepest appreciation to Prof. Eiji Goto. Throughout my Ph.D. journey, Prof. Goto has provided me with invaluable guidance, patient instruction, valuable advice, and endless care. His expertise, dedication, and trust in me have been instrumental in shaping my academic growth, and I will forever be grateful. Especially during the process of revising journal papers, I learned many qualities essential to becoming an excellent scientist. I hope to become as outstanding a scientist as Prof. Goto in the future. I am also very grateful to Prof. Goto for providing all the equipment, including computers, software, experimental shelves, and all the measuring instruments, among others. Without these, I would not have the opportunity to conduct interesting research and achieve good results. Most importantly, Prof. Goto has taught me courage and diligence, encouraging me to pursue endeavors even in the face of possible failure, and to focus on enjoying the research process without being overly concerned about outcomes. His guidance has equipped me with problem-solving skills applicable to various challenges, not limited to academic pursuits. I am confident that these will continue to influence my future career and life endeavors.

In addition, I sincerely appreciate Prof. Nobuhiro Matsuoka and Prof. Masahumi Johkan for taking time to review the thesis, raising many valuable comments. These comments are all valuable and very helpful to improve the thesis.

Furthermore, I extend my thanks to the Prof. Shoko Hikosaka. Her support has provided crucial assistance to my research work. I am immensely grateful for her gentle and compassionate care. At the same time, she has been inspiring me to be courageous in becoming an outstanding female researcher.

Moreover, I would like to express my gratitude to Prof. Hideo Yoshida, for his enthusiasm, help, and professionalism. I am equally grateful to my lab colleagues for their helpful advice.

I am also grateful to Prof. Rui Wang. Without her, I would not have the opportunity to come to Japan and improve myself on a best platform. Additionally, I appreciate the Ministry of Education, Culture, Sports, Science and Technology (MEXT) and China Scholarship Council (CSC). Their support through the scholarship allowed me to focus on the studies without distractions.

I am also deeply grateful to my family and friends for their unwavering support and encouragement throughout my Ph.D. journey. Their understanding, support, and encouragement have been my driving force.

Finally, I want to thank all those who have helped and supported me along the way. It is your support and assistance that have enabled me to successfully complete my Ph.D. program. Let us celebrate this achievement together and witness my growth and progress.